

REPORT DOCUMENTATION PAGE

Form Approved
OMB No. 0704-0188

The public reporting burden for this collection of information is estimated to average 1 hour per response, including the time for reviewing instructions, searching existing data sources, gathering and maintaining the data needed, and completing and reviewing the collection of information. Send comments regarding this burden estimate or any other aspect of this collection of information, including suggestions for reducing the burden, to the Department of Defense, Executive Service Directorate (0704-0188). Respondents should be aware that notwithstanding any other provision of law, no person shall be subject to any penalty for failing to comply with a collection of information if it does not display a currently valid OMB control number.

PLEASE DO NOT RETURN YOUR FORM TO THE ABOVE ORGANIZATION.

1. REPORT DATE (DD-MM-YYYY) 5 Aug 2008		2. REPORT TYPE Final Report		3. DATES COVERED (From - To) 1 May 06-30 Sept. 10	
4. TITLE AND SUBTITLE Self-Assembled Soft Optical Negative Index Materials Overview			5a. CONTRACT NUMBER FA9550-06-1-0337		
			5b. GRANT NUMBER		
			5c. PROGRAM ELEMENT NUMBER		
6. AUTHOR(S) Prof. Peter Palffy			5d. PROJECT NUMBER		
			5e. TASK NUMBER		
			5f. WORK UNIT NUMBER		
7. PERFORMING ORGANIZATION NAME(S) AND ADDRESS(ES) Kent State University Office of the Comptroller Horning Rd Kent, Ohio 44242-0001			8. PERFORMING ORGANIZATION REPORT NUMBER		
9. SPONSORING/MONITORING AGENCY NAME(S) AND ADDRESS(ES) Air Force Office of Scientific Research 875 North Randolph Street Arlington, VA 22203			10. SPONSOR/MONITOR'S ACRONYM(S)		
			11. SPONSOR/MONITOR'S REPORT NUMBER AFRL-OSR-VA-TR-2013-0932		
12. DISTRIBUTION/AVAILABILITY STATEMENT Distribution Statement A: Approved for public release. Distribution is unlimited.					
13. SUPPLEMENTARY NOTES					
14. ABSTRACT The current focus of the research is aimed at quantifying blue-shift variations and the enhanced resonance intensity as the nanorod gap size is changed. Advances in the surface functionalization techniques are also being investigated to control gap spacing in the 5-25 nm range. There is an indication that it may be possible to produce suspensions of self-assembled equilateral triangles composed of three Au nanorods. If this process does work it would provide the first 2-D fluid of nanoscale SRR structures, the first step towards realizing the desired tetrahedral structure that is theoretically envisioned					
15. SUBJECT TERMS					
16. SECURITY CLASSIFICATION OF:			17. LIMITATION OF ABSTRACT	18. NUMBER OF PAGES	19a. NAME OF RESPONSIBLE PERSON
a. REPORT	b. ABSTRACT	c. THIS PAGE			19b. TELEPHONE NUMBER (Include area code)

20130918324

Final Report MURI06: Self-Assembled Soft Optical Negative Index Materials

Overview

The goal of this MURI, as outlined in the original proposal, was the realization of bulk 3D negative index materials (NIMs), where the negative index is the result of negative bulk permittivity and permeability in the VIS-IR range.

The MURI team consisted of a multidisciplinary team of 13 scientists:

<i>David Carroll</i>	Physics, Wake Forest U., nanotechnology, optics
<i>Sharon Glotzer</i>	ChemE & MSE., U. Michigan, self-assembly simulations
<i>Leslie Greengard</i>	Courant Inst., NYU, numerical modeling of optics
<i>Nicholas Kotov</i>	Chem. Eng., U. Michigan, nanotechnology, self assembly
<i>Oleg Lavrentovich</i>	Liq. Crist. Inst., Kent State U., electrooptics, self assembly
<i>Quan Li</i>	Liq. Crist. Inst., Kent State U., surfactant synthesis
<i>Sia Nemat-Nasser</i>	Mechanical Engineering, UCSD, 3D microwave materials/models
<i>Peter Palffy-Muhoray</i>	Liq. Crist. Inst. Kent State U. optics, material characterization.
<i>Sheldon Schultz</i>	Physics, UCSD, nanoparticle spectroscopy
<i>Costas Soukoulis</i>	Physics, Iowa State; Ames Lab, theory, modeling
<i>Bahman Taheri</i>	AMI, Inc., LCI, Kent State U, processing, optics (industry)
<i>Eric Van Stryland</i>	CREOL, UCF, Nonlinear optics

The originally envisioned materials were dispersions of metallic nanoparticles in a host matrix. The negative response was to be realized through the individual response of nanoparticles, while the key negative permeability was to be realized through the collective response of assembled nanoparticles. The nanoparticles were to be orientationally ordered, forming a liquid crystal phase, and the host material itself may also be liquid crystalline. Materials were to be created via self-assembly of nanoparticles with functionalized surfactants/tethers, and subsequently processed to form large area thick 3D films. As a consequence of liquid crystallinity, these NIMs were expected to be soft and responsive, allowing easy processing and switchability.

In essence, all of the goals of the project were realized; however, they were realized subject to a fundamental and dramatic constraint: the constraint imposed by inherent losses. This game changing constraint was not well known in the research community when our proposal was submitted; we became aware of its possibility and pointed it out first at the MURI kick-off meeting at the University of Michigan in Fall 2006. The proposed prospect of large inherent losses was originally met with considerable skepticism, but subsequently became well established¹ and fundamentally changed research in the field.

Seven universities participated in the MURI with some 13 PIs, bringing a wide variety of expertise. Their contributions are summarized in the body of the report; highlights (in

alphabetical order of institutions) are as follows. The ISU team designed metamaterial structures capable of exhibiting NIM and hyperbolic dispersive behavior, exploiting chirality to realize NIM, and advancing our understanding of Casimir forces in chiral and non-chiral metamaterials. The KSU group, together with UM, developed methods to produce and process Au NR based 3D metamaterials, including the developed new Au LC phases, and provided sample materials for much of the MURI effort. KSU developed and carried out extensive characterization, worked with NYU to connect numerical modeling to experiment, and provided both administrative and technical guidance for the MURI project. The NYU group developed a new numerical method, the Fast MultiParticle Scattering (FMPS) which can accurately compute the numerical response of non-periodic metamaterial systems. This is one of the key contributions of the MURI to the community. The UCF group characterized the nonlinear optical response of the metamaterials developed during the project and explored the nonlinear enhancement. One of the UCSD teams characterized individual NPs to complement the KSU work on bulk composites and also to test and confirm the accuracy of theoretical models provided by ISU. The second UCSD team worked on 3D microwave model systems to test, experimentally, metamaterials designed by the ISU team. Both hyperbolic dispersion and a chirality-based response were confirmed. The UM team consisted of two collaborating groups, one developing new NPs with novel shapes, composition and properties and studying their aggregated structures, while the other carried out computer simulations NP self-assembly. The demonstration of quasicrystal formation by hard tetrahedra is a key fundamental result of the project. WFU created parallel arrays of Au and Ag NWs as well as other structures using anodized Al templating, and demonstrated hyperbolic dispersion.

The fundamental limitation of inherent dissipative losses, due to the basic underlying physics, has prevented the realization of large aperture ‘perfect’ lenses which was one of the goals of this MURI and of many other research efforts. In addition to understanding this mechanism, many important scientific advances were made under this MURI. In addition to the published literature, these are summarized in the main body of the report.

Iowa State University

PI: Costas Soukoulis

Optical anisotropic metamaterials for negative refraction and focusing

Early on in the project, our focus was on finding metamaterial structures that can self-assemble and work at optical frequencies. Experimental results from within the MURI indicated that anodization of aluminum films provides hexagonal nano-hole arrays, which, when backfilled with e.g. silver via electro deposition can provide highly uniform films of metallic nanowires which are aligned perpendicular to the films surface. From earlier theoretical work done in our group it was known that arrays of parallel thin wires could provide metamaterials that behave as indefinite media with hyperbolic dispersion – although there existed some controversy in the community about this claim. Therefore, we decided to develop and simulate an optical indefinite

anisotropic wire medium at optical frequencies that would be realistic and promise the possibility of experimental implementation.

Fig. 1 below illustrates the concept of negative refraction provided by an indefinite anisotropic medium. When the material parameters (permittivity or permeability) parallel and perpendicular to a given surface of the medium have different sign, the normally elliptic EFS of the anisotropic material changes into a hyperbola. This has two consequences: First, negative refraction occurs at the interface for the group velocity (i.e. direction of the beam, indicated by red arrow) because it is related to the gradient of the dispersion, standing perpendicular to the EFS. At the same time, the phase velocity refraction remains positive. Both can be clearly observed in the right panes of Fig. 1 showing the full-wave simulation results (FEM simulations using COMSOL). Second, the hyperbolic dispersion converts modes with high parallel momenta that are evanescent in air into propagating modes inside the medium. This enables super-resolution imaging and/or focusing because evanescent modes are not lost while propagating through the metamaterial.

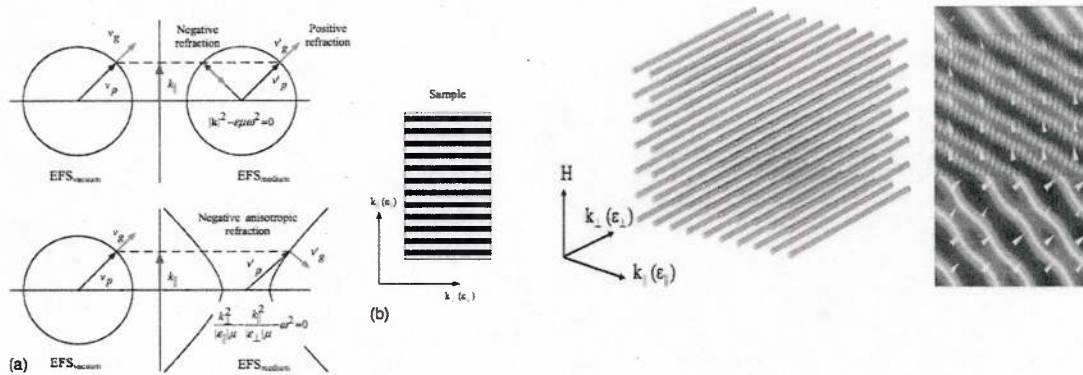


Fig. 1: The left panel illustrates the idea of obtaining negative refraction by virtue of an indefinite metamaterials. A nanowire metamaterial with positive permittivity parallel to the surface and negative permittivity perpendicular to the surface possesses a hyperbolic EFS which supports negative refraction and super-resolution imaging. The right panel shows a schematic of the nanowire material and the actual simulated field distribution for the optical nanowire metamaterials showing negative refraction for the group velocity (white arrows).

In detailed simulations we demonstrated that such an indefinite anisotropic metamaterial that homogenizes as an effective medium with hyperbolic dispersion is possible and can be implemented using gold or silver nanowires. The metamaterial we designed uses square or hexagonal arrays of thin (10–20nm diameter) nanowires with lengths of the order of micrometers embedded in air or in an alumina matrix and operates for light of about 700nm (red, visible light) wavelength.

Fig. 2 shows the dependence of the effective permittivity as function of the radius of the nanowires, which follows nicely the Maxwell-Garnett effective medium theory. This is a very desired behavior because it provides quantitative predictability.

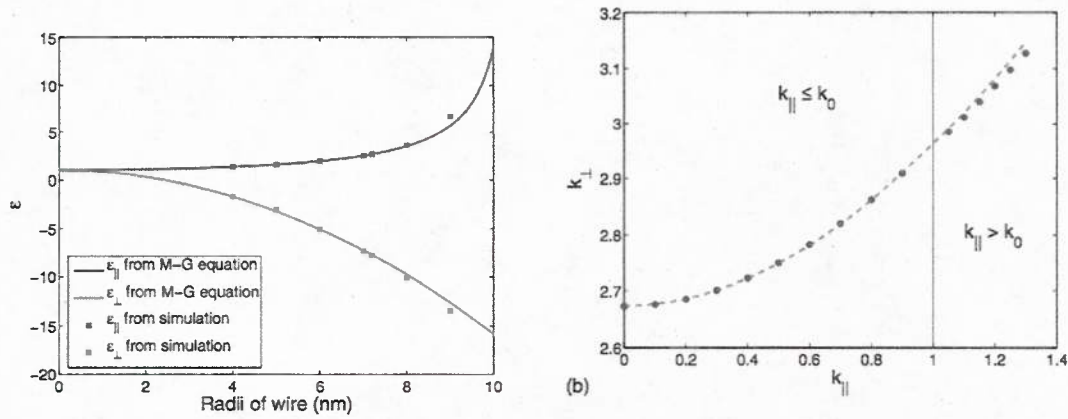


Fig. 2: The left panel shows the retrieved effective anisotropic permittivity tensor components as a function of the radius of the wires. For this optical nanowire metamaterial the simulated results (points) closely follow the homogeneous medium in Maxwell-Garnett approximation. In the right panel the retrieved hyperbolic dispersion relation is shown. The points are the simulation results, the dashed line the fit to the hyperbolic EFS formula shown in Fig. 1. The last six point of the curve demonstrate that the hyperbolic dispersion holds for evanescent waves as well, allowing for super-resolution imaging.

The right panel in Fig. 2 show the dispersion relation retrieved from the simulation data, which proves, (a) that the medium indeed has hyperbolic dispersion, and (b) that the hyperbolic dispersion holds well into the evanescent modes.

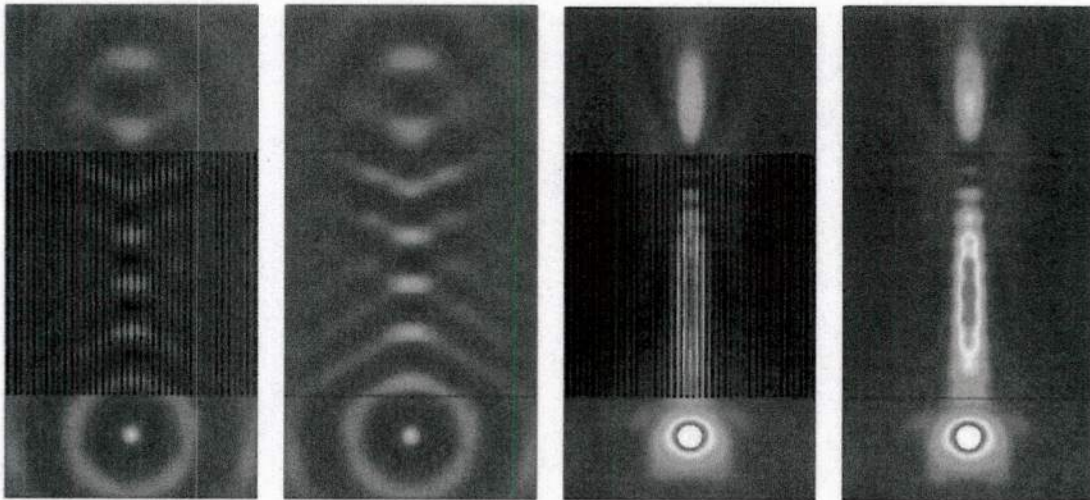


Fig. 3: The field (left two panels) and intensity (right two panels) distributions of a point source (bottom) in front of the effective hyperbolic anisotropic nanowire optical metamaterials operating at a wavelength of 700nm are shown. The first and third panels show the simulation results for the nanowire metamaterial, the second and last panel the corresponding homogenous

medium distributions using the fitted dispersion relation. This proves that the nanowire medium indeed behaves as effective metamaterial with hyperbolic dispersion.

This is important, as it allows for super-resolution. Eventually, for high enough parallel momenta, this property is destroyed because of the non-zero lattice constant of the nanowire array.

Fig. 3 shows the ultimate test for our theory and the designed optical metamaterial. Using the data from the retrieved dispersion fitted to the theoretical dispersion relation, we compare the simulated field and intensity distributions for the actual metamaterials with a homogeneous anisotropic medium, the permittivity tensor of which is given by the fitted dispersion relation. The pictures show the imaging of a point source placed in front of the medium and are in perfect agreement between theory and simulation. This proves beyond any doubt, that the optical anisotropic wire array metamaterial indeed homogenizes as an effective medium with hyperbolic dispersion.

Our results have been published in Physical Review B [1].

Chiral resonators for chiral metamaterials and repulsive Casimir force

A second major topic investigated by our group is the exploration and testing of chiral metamaterials. Chiral metamaterials have been proposed as an alternative route to negative refraction. As shown by theory, negative refraction can be obtained for one of the two circularly polarized propagating eigen modes (plane wave solutions) without the requirement for simultaneously negative effective permittivity and permeability, provided that the chiral response function κ can be made large enough. This allows for much simpler nano-resonator structures than in conventional “double negative” metamaterials. Also potentially lower losses (as only one resonance is needed instead of two) have been attributed to chiral metamaterials. Besides the above, we have a major interest in chiral nano-resonators for self-assembled optical metamaterials because of their structural simplicity and compactness – individual resonators are independent units of a single species and can (theoretically) be freely distributed in space. This is a big advantage over “double negative” metamaterials which typically require two resonator species (one electric and one magnetic) or long (continuous) wires. Although, we have also done some effort to combine both resonance into a single nano particle (e.g. “tuning-fork” resonators).

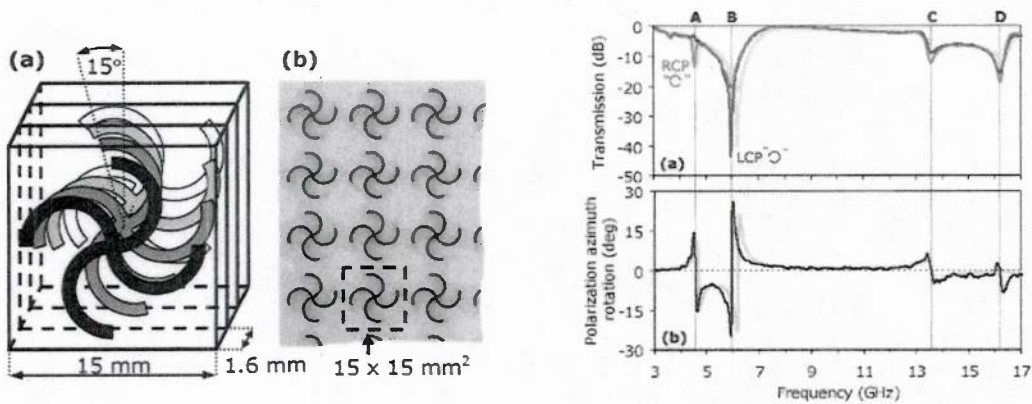


Fig. 4: Chiral metamaterial design base on successively twisted rosettes. The resonator structure and a microwave implementation are shown on the left; the transmittance for RCP and LCP plane waves as well as the huge optical activity are shown on the right.

The first metamaterial structure we could demonstrate to provide a negative refractive index was a rosette shaped metallic resonator with successive individual units twisted either in a right-hand or in a left-hand sense. For this structure we were able to prove in simulations and in microwave experiments that the obtained negative index was due to the large resonant chirality parameter κ rather than simultaneously negative effective permeability and permittivity. This work was performed in collaboration with N.I. Zheludev's group in the UK. Results have been published in Physical Review B [2].

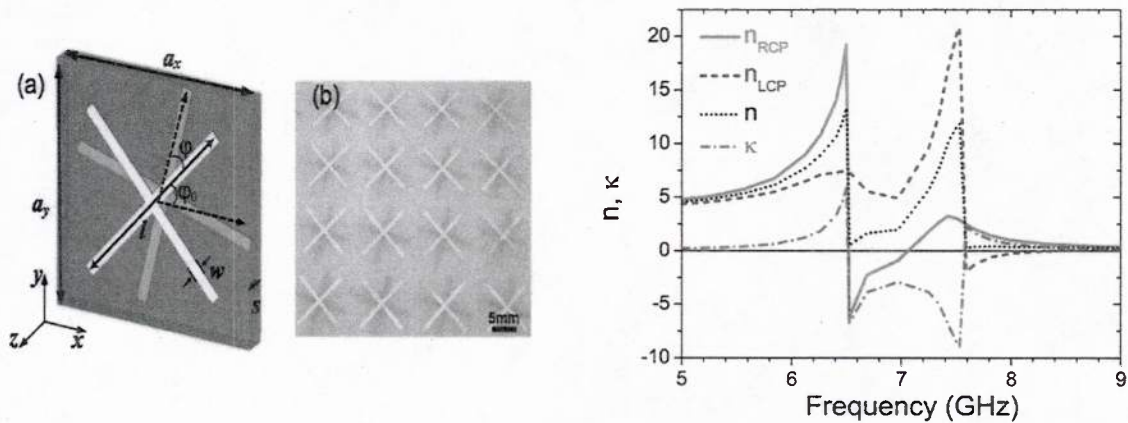


Fig. 5: Resonant chiral response can be achieved with simpler crossed-wire structures. As the retrieved parameters shown in the right panel demonstrate, the negative index of the circularly polarized eigenmodes is due to the chirality (coefficient κ , green line).

Further investigation by our group revealed that much simpler pairwise straight cross-wire resonator can be used to the same effect. An example is shown in Fig. 5 above and has been confirmed by microwave experiments performed by us at Iowa State University. It can clearly be

seen from the retrieved effective refractive index in the right panel that the refractive index for the RCP or the LCP mode becomes negative because of the resonance in the chiral parameter κ (green curve) while the refractive index due to the diagonal response functions (permeability and permittivity) remains positive (black curve).

These results were published in Physical Review B [3].

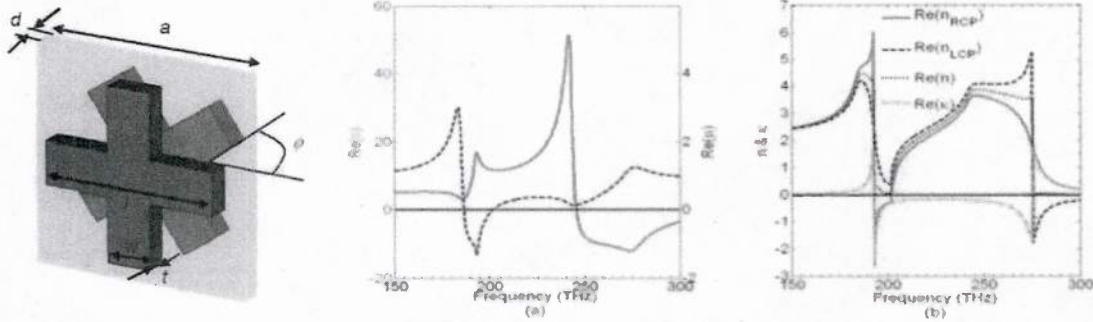


Fig. 6: Optical chiral resonator working at communication frequencies around 1.5 μ m. The left panel indicates the structure, the right panel shows simulation results for permittivity, permeability, as well as the refractive indices for the circularly polarized eigenmodes.

The cross-wire chiral resonator can be scaled to optical frequencies. Results for a negative index chiral metamaterial based on this design, which operates at the telecommunication wavelength of 1.5 μ m in the near infrared, is shown in Fig. 6 and has been published in Optics Express [7].

We also investigated chiral resonator designs, which are based on pairs of intercalated short spiral segments and have the advantage over the previous designs that they are more compact, and can be made deeper subwavelength, i.e. with a larger operating-wavelength to unit-cell-size ratio which is very important for the homogenization of the metamaterial as an effective homogenous medium. Again, results of simulations and microwave experiments as a prove-of-principles are shown in Fig. 7 and have been published in Applied Physics Letters [5]. A review of recent chiral approaches to negative refraction was published in Journal of Optics A [4].

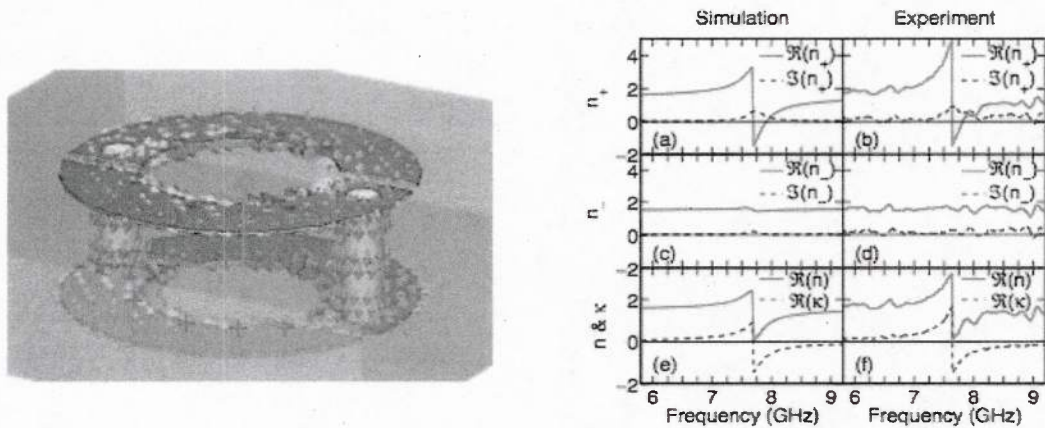


Fig. 7: Chiral resonators can be realized by non-planar structures. An example of a chiral ring structure, comprised of two interlocked spirals, is given in the left panel. The right structure shows simulation and experimental results for a two dimensional arrangement of such resonators providing negative index due to chirality.

Realistic chiral materials are still based on a resonant response and conducting metallic structures providing this resonant chiral susceptibility. As a consequence, they typically become very lossy (as ordinary metamaterials do as well) when used close to their resonance frequency. As can be seen in Fig. 8, this usually unwanted loss can be turned into a benefit when constructing a perfectly absorbing metamaterial. The chiral absorber we developed takes advantage of the chiral response to provide polarization-independent near-unity absorbance, which is also nearly independent of the incidence angle. The very simple design is based on a single layer of chiral resonator as shown in Fig. 7, backed by an reflecting back plane. The Results were published in Physical Review B [6].

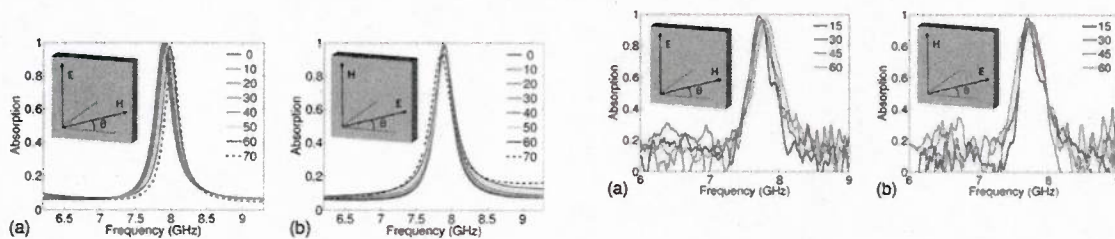


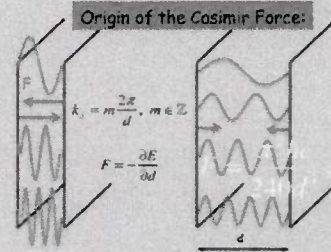
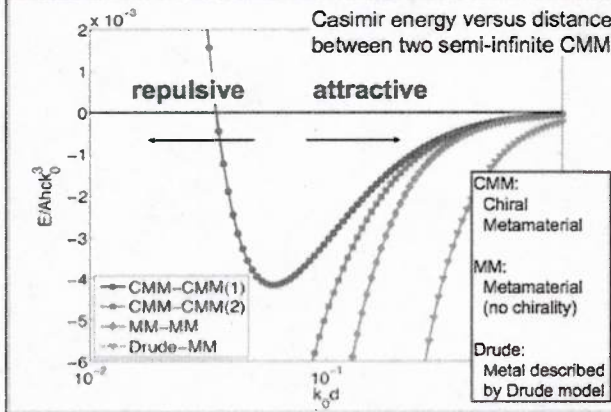
Fig. 8: Near-perfect, angle- and polarization-independent absorber realized with chiral metamaterial. The left panel shows simulation results, the right panel microwave experimental data.

There is another reason for the widespread interest in chiral metamaterials: Independent work in our group recently discovered that chiral metamaterials could be useful to minimize or even reverse the attractive Casimir force in micromechanical structures.

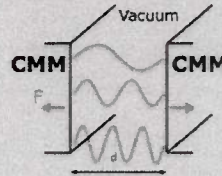
Chiral metamaterials for repulsive Casimir force

We extended Lifshitz theory to calculate Casimir energy per area:

$$\frac{E(d)}{A} = \frac{\hbar}{2\pi} \int_0^\infty d\xi \int \frac{d^2 \mathbf{k}_\perp}{(2\pi)^2} \ln \det(1 - \mathbf{R}_1 \cdot \mathbf{R}_2 e^{-2Kd}), \quad (\xi = -i\omega)$$



The Casimir force is the derivative of the Casimir energy. It becomes repulsive if the chiral response function becomes sufficiently large



$$\epsilon = \epsilon_0 + \frac{\Omega_c \omega_0^2}{\omega_0^2 - \omega^2 - i\omega\gamma}$$

$$\mu = \mu_0 + \frac{\Omega_c \omega^2}{\omega_0^2 - \omega^2 - i\omega\gamma}$$

$$\kappa = \frac{\Omega_c \omega_0 \omega}{\omega_0^2 - \omega^2 - i\omega\gamma}$$

Fig. 9: Illustration of repulsive Casimir force between chiral metamaterials.

The Casimir force quantum-mechanical in nature, arising from the zero-point energy of the quantized electromagnetic field modes trapped between conducting or polarizable microstructures. This attractive force is highly undesirable in micromechanical systems as it leads to “stickiness” and friction between components. Between chiral media, the Casimir force can be made repulsive (or, at least greatly reduced), if the chirality becomes sufficiently large, because of the off-diagonal degrees of freedom in the reflection amplitudes of the chiral media. An illustrative overview is given in Fig. 9 above; more details can be found in Phys. Rev. Lett. 103, 103602 (2009).

Using our expertise with the development of chiral resonators and chiral metamaterials acquired also during this MURI, we investigated how currently available chiral resonator designs – most of which invented by our group, like the straight cross-wire pairs and the conjugate swastika resonators – could perform with respect to meeting the conditions for a repulsive Casimir force. An overview of the results is provided in Fig. 10. None of the designs provide chirality strong enough to reverse the sign of the Casimir force. However, significant reduction of the attractions is possible and the most promising designs turned out to be the 4-U and the conjugate swastika structure. Unfortunately, these structures are too complicated and structurally too sensitive to tolerances to be useful for the self-assembly approach. Our findings have been published in Physical Review B [11].

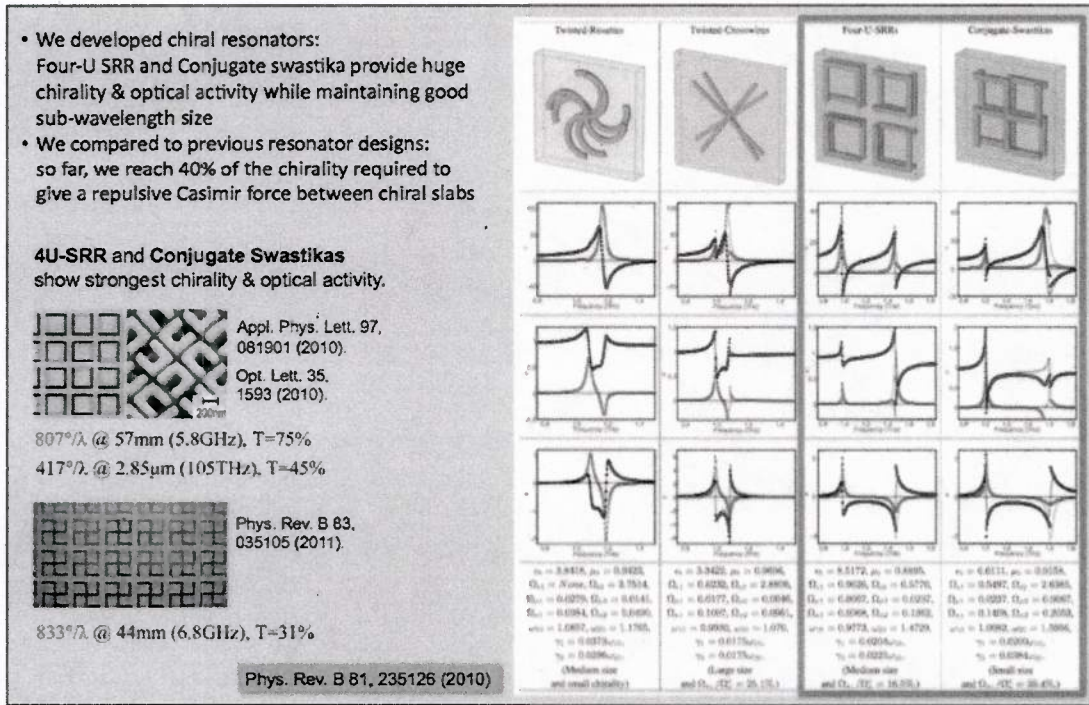


Fig. 10: Comparison of several chiral metamaterial designs with respect to their suitability to implement a repulsive Casimir force.

Optical forces in nanowire pair magnetic resonators

The most common building block for current –and likely most future– self-assembled optical metamaterials are rod-shaped nanowires of various lengths and aspect ratios. They are ubiquitous, easy to synthesize or buy and a wealth of knowledge has been accumulated about their use and self-assembly. However, in contrast to fixed lithographic structures, self-assemble nanostructures retain a dynamical degree of freedom as the constituents can move – under external forces as well as under the optical forces caused by the electromagnetic field itself. Additionally, as nano-resonators are resonant structures the optical forces are substantially amplified by and do strongly depend on the characteristics of those resonances. It is therefore essential to understand the optical forces acting on these nano-resonators.

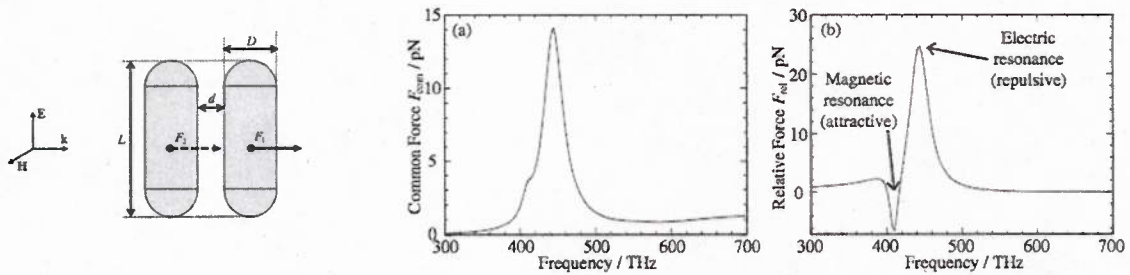


Fig. 11: A nano-rod pair as used for magnetic resonators for optical metamaterials (left) as well as the common and relative components of the optical force acting on the nano-rod pair if excited around its lowest two resonant modes by an incident plane wave.

We have studied the optical forces on nano-rod-pair resonators using a Maxwell stress tensor formalism together with finite elements simulations. The forces in nano-rod pairs can be much stronger than the forces on nano-spheres because of the larger polarizabilities. We observed that the optical force is strongly enhanced around the resonant eigen modes and that the sign of the force depends on the symmetry of the mode but also on the arrangement of the nano-resonators. There is an electric (charge-charge Coulomb force) and a magnetic (current-current Lorentz force) contribution to the relative optical force in the nano-resonators. For an sufficiently isolated nano-resonator, the electric component is dominant and attractive for the magnetic resonance (anti-parallel linear currents in the two nano-rods, magnetic current-current force is repulsive) and repulsive for the electric resonance (parallel linear currents). This is clearly visible from the right panel in Fig. 11. The situation changes dramatically if we consider periodic arrangements of nano-rod pairs: Now the periodicity allows the balance between the electric and magnetic contribution to the relative force to be shifted depending on the separation. If we scan the separation of the rods in the nano-rod pair we can observe even the sign of the force to change from repulsive to attractive as shown and illustrated in Fig. 12. The reason for this behavior has been identified in the changing balance of magnetic and electric contribution to the relative optical force and the screening of the coulomb contribution for dense wires by the periodicity. These results and detailed parametric studies have been published in Optics Express [12]. The finding will have to be taken into account to achieve sufficiently stable self-assembly of optical metamaterials. On the other hand, the optical force also provides an avenue to implement strong non-linear optical response.

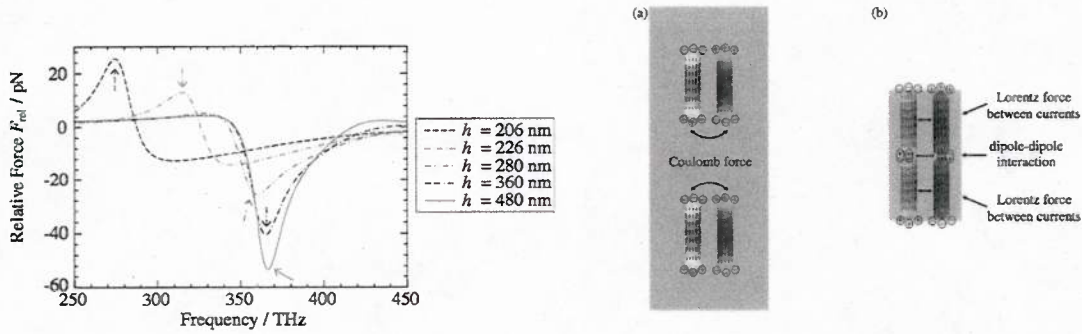


Fig. 12: Relative optical force in periodically continued nano-rod resonator for different axial distance between the nano-rods. The arrow indicates the position of the magnetic resonance. The panel on the right illustrates the change in the balance of electric and magnetic contribution to the optical force, which leads to the sign change from attractive to repulsive for sufficiently dense resonator packing.

Metamaterial resonators from non-resonantly couples surface modes

Most metamaterial designs are based on spatially distributed but discrete resonators, particularly for the magnetic response. The magnetic resonators are typically of the SRR type, employing an inductive current loop in combination with a restoring force provided by the capacitance of a gap in the current path. One of the two main issues (the other being dissipative loss) with these resonator types is the failure of geometric scaling and the saturations of the resonance frequency at small length scales, i.e. high (optical) frequencies. We investigated and implemented an entirely new concept for the generation of resonant electric and magnetic response in metamaterials: Instead of magnetic SRR or electric cut-wire type resonators we employ delocalized resonant states, like surface modes, e.g. on thin metal films, to provide the resonant local energy storage mechanism. Then, using conceptually non-resonant scatterers, we couple the “dark” resonant state to the propagating fields. Whether an electric (permittivity), magnetic (permeability), or arbitrary other response (e.g. chiral) is obtained, solely depends on the structure and symmetry of the non-resonant scatterers, which act like little antennas coupling the propagating waves to the local resonant near-fields. In Fig. 13, we show two prototypical examples, implementing a magnetic resonator with resonant (and negative) permeability (left panel) and an electric resonator with resonant (and negative) permittivity (right panel), both of which use the same symmetric surface plasmon of a thin metal film as the actual resonant state.

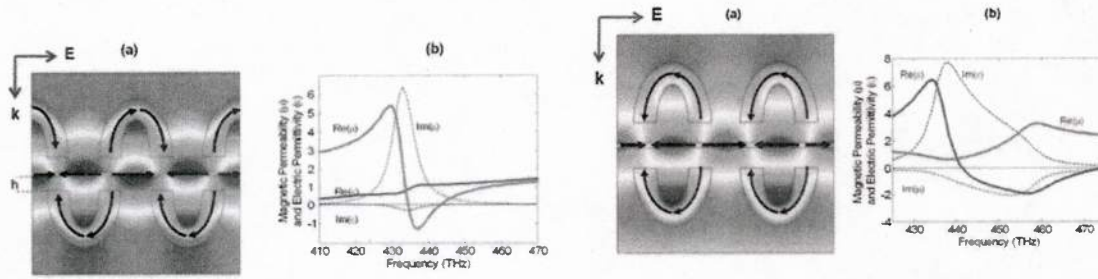


Fig. 13: Simulated field distributions and retrieved effective material parameters for the magnetic resonator with response in the permeability (left panel) and the corresponding electric resonator with response in the permittivity (right panel). Both are based on the resonance provided by the delocalized surface plasmon on the thin metallic film.

The most important advantage of this approach is that the scaling of the delocalized modes can be substantially different from that of compact resonators like SRRs. This may potentially pave the way to magnetic response in the ultraviolet. Results have been published Physical Review B [13].

Magnetic resonance from oriented nanowire double-layers

Most recently, we investigated the dependence on the electric and magnetic resonance frequencies as well as the corresponding absorption on the geometrical parameters in ordered nano-rod double layers as illustrated in Fig. 14. These structures are interesting, as they seem to be relatively easily obtainable experimentally with widely tunable geometry of the nano-rods. Remarkably, the resonance frequencies only weakly depend on the in-plane height & width of the unit cell of the periodic arrangement. This is fortunate since the strong resonant response desired in order to drive permeability and permittivity negative in common negative index metamaterial designs requires dense packing of resonators with high volume filling ratios. The strength of the magnetic resonance also increases with the separation between the layers up to a point. This is expected as the magnetic dipole moment of the nano-rod pairs increases with the enclosed area, i.e. distance between the layers. However, if the distance gets too large and becomes comparable with the wavelength the magnetic resonance is eventually destroyed.

Other activities within the MURY effort have been the investigation of the attainable negative index in weakly vs. strongly coupled stratified optical metamaterials, published Physical Review B [8]. Also the feasibility of geometric means of loss reduction and connected bulk optical metamaterials were studied. Results have been published in Physical Review B [9] and Optics Letters [10], respectively.

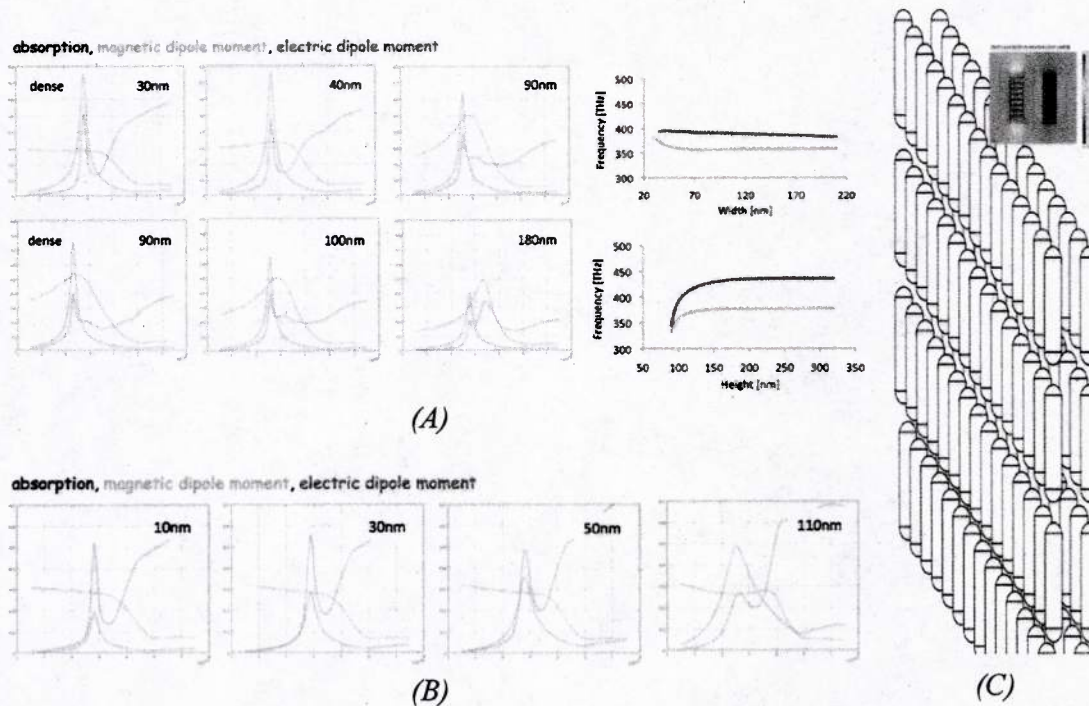


Fig. 14: Magnetic response of a nano-rod double-layer, schematically illustrated on the right (C). The dependence of the absorption, electric & magnetic dipole moment as a function of the in-plane width (top) and height (bottom) is shown in panel (A); the corresponding dependence on the separation between the two layers is shown in panel (B).

Kent State University

PI: Peter Palffy-Muhoray, Co-PIs: Oleg Lavrentovich, Quan Li, Bahman Taheri

The KSU effort was multifaceted, ranging from the synthesis, processing, characterization, theoretical and numerical modelling and device production.

Synthesis

Synthesis of Au NRs was developed and carried out at KSU in close collaboration with Kotov at UM. Initial synthesis of surfactants was carried out by Quan Li. He demonstrated the ability to produce ionic, polymeric, chiral and mesogenic as well as azo-based surfactants. However, these were not produced in sufficient quantities to enable use by the MURI group. Consequently, Li left the MURI team in 2009. Kotov and the KSU group developed efficient and controlled synthesis procedure for Au NRs, thiolated polymeric surfactants and phase transfer methods. These enabled the production of stable colloidal suspensions of AuNRs of given size and aspect ratio, both in aqueous and organic solvents. This allowed the efficient production of a wide range of bulk Au NR metamaterial samples which were subsequently studied by the MURI team.

Demonstration and control of self-assembly of Au NRs via chromonic liquid crystals

Lavrentovich and Kotov

In a collaborative effort, a new approach was developed for the controlled non-covalent assembly of Au NRs via polyionic self-assembled stacks of organic chromonic molecules. Depending on the charge of the gold nanorods, the chromonic stacks assemble them either end-to-end or side-by-side through anisotropic attractive forces. This method has a number of advantages over the recently discovered other techniques based on covalent binding and usage of biopolymers; it is universal, robust, based on new principles of linker-nanorod interactions and allows the researchers to gradually control the degree of NR assembly by controlling the chromonic self-assembly, for example, by changing the concentration or pH of the solutions. The mechanisms enabling the assembly are closely related to the mechanisms of condensation of like-charged rods of biological polyelectrolytes (B-DNA, f-actin, etc.). Results are expected to be of interest to materials scientist, ranging from those who study condensation of biopolymers and formation of liquid crystalline phases in self-assembled lyotropic systems, to those who develop colloidal NRs systems for metamaterials, sensors, cloaking devices, etc. The results [14] offer compelling end-to-end assembly of NRs that could soon provide the route to site-specific functionalization.

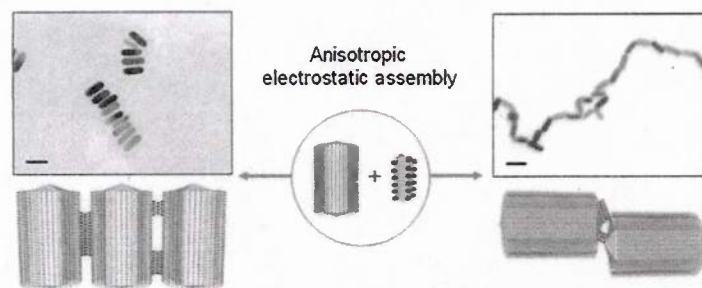


Fig. 15. Side-to-side and end-to-end assembly of Au NRs via chromonic liquid crystals.

Electrically reconfigurable optical metamaterials

Lavrentovich developed electrically reconfigurable colloidal suspensions of Au NRs, where electric field gradients changed the concentration and orientation of Au NRs [15-17]. The resulting change in optical properties was similar to cloaking strategies suggested by V. Shalaev and others, and effectively cloaked part of the image in the cell. The results suggest that such an approach can lead to the realization of certain types cloaking devices.

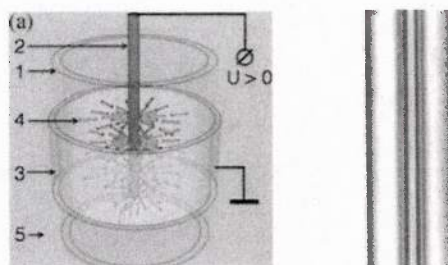


Fig. 16. Electrodes and Au NRs under an applied electric field (left), and image of the system; the central electrode becomes nearly invisible when field is ON.

First Liquid Crystal Phase of Au NRs.

Palffy-Muhoray

Based on simple theoretical arguments and numerical simulations, sufficiently dense assemblies of Au NRs are expected to show hyperbolic dispersion, and, for certain specific structures, negative refraction. The challenge is to achieve oriented samples with a sufficiently high volume fraction (>30%) NRs without aggregation and while maintaining the plasmon resonances of the individual NRs. By using thiolated polystyrene surfactants on Au NRs with aspect ratio ~ 5 and linear/cyclic polymer solvents, high volume fraction colloidal NR suspensions were realized. The samples are birefringent viscous liquids, which can be reoriented with an electric field, and represent the first observation of a liquid crystal phase of metallic NRs. If the volume fraction can be increased sufficiently, subject to the above constraints, these materials are expected to show negative refraction. Work to realize this is underway.

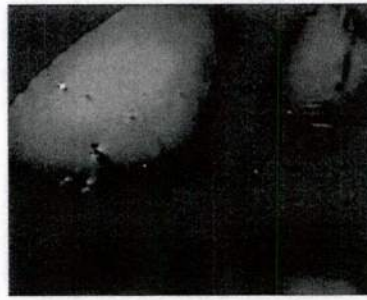


Fig. 17. Micrograph of Au NR nematic LC between crossed polarizers.

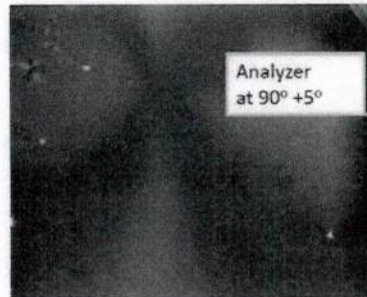


Fig. 18. Micrograph of Au NR nematic LC

Determination of Au NR suspension susceptibility

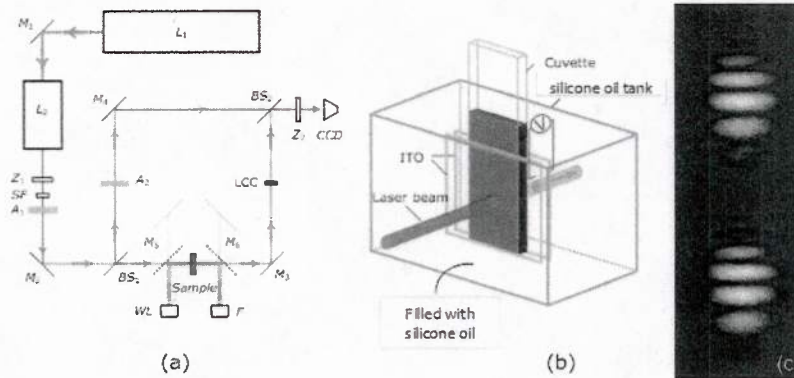


Fig. 19 (a) Mach-Zehnder interferometer with integrated spectrometer for phase shift measurements (b) cuvette under applied electric field immersed in silicone oil to prevent dielectric breakdown. Sample interferograms taken at two different concentrations (c).

The key contribution of KSU was the experimental determination of the susceptibility of Au NRs in colloidal suspensions. Using a specially built Mach-Zehnder interferometer with an integrated spectrophotometer, the real and imaginary parts of susceptibility tensor for Au NRs in an orientationally ordered suspension were measured as a function of wavelength and concentration for the first time. This characterization enables the comparison of the measured response with theory and exact numerical models. It is found that the experimental results are in

good agreement with the predictions of theory. The results are summarized in the graphs below in Figs. 20 and 21.

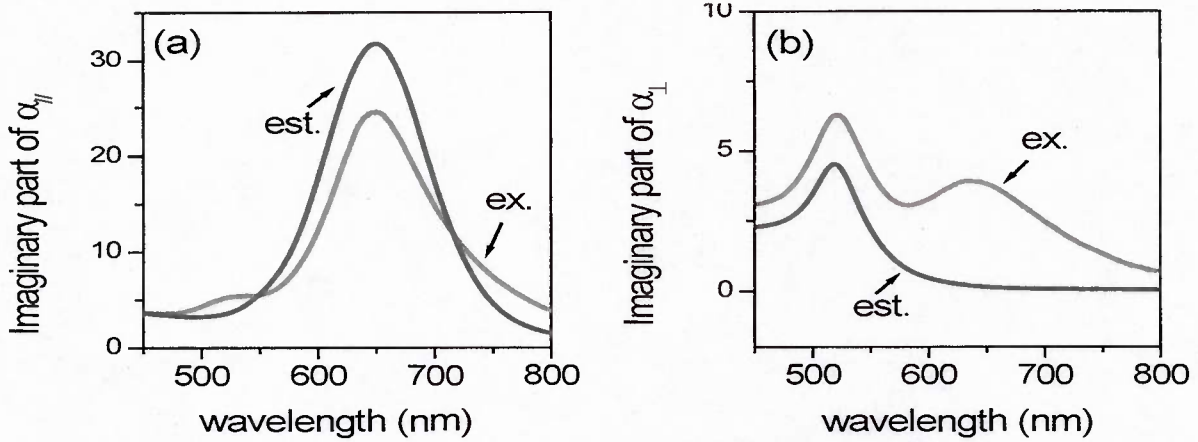


Fig. 20 Imaginary parts of the susceptibility (a) parallel and (b) perpendicular to the applied aligning electric field. Plots show experimental results (red curves) at $\phi_v = 2.72 \times 10^{-5}$ and the corresponding predictions of modified Rayleigh-Gans theory (blue curves).

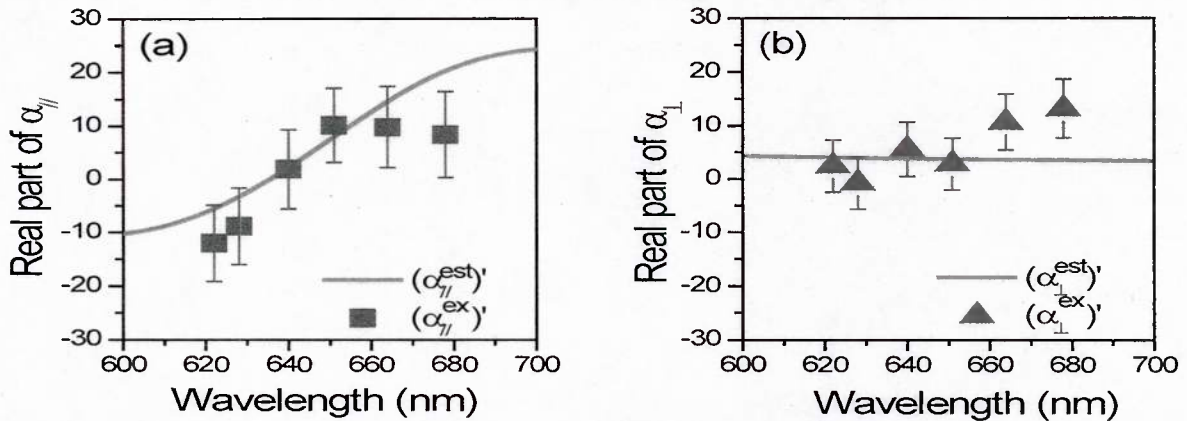


Fig. 21 Real parts of the polarizability (a) parallel and (b) perpendicular to the applied aligning electric field. Plots show experimental (symbols) results at $\phi_v = 2.72 \times 10^{-5}$ and the corresponding predictions of modified Rayleigh-Gans theory (red curves).

Losses in metallic metamaterials at optical frequencies.

The main result of the measurements is that the optical response of Au NRs in bulk is in accord with theoretical predictions. It agrees with numerical calculations for individual NRs as carried out by the NYU group via FMPS scheme, and with simple approximate model predictions H5-H7.

Dissipative Losses and their Role

Palffy-Muhoray

As the experimental measurements and NYU numerical simulations clearly show, plasmon resonance of Au NRs is well described by a simple classical harmonic oscillator model. To achieve negative polarizability, the optical field must be at shorter wavelengths than the longitudinal resonant mode. To achieve negative ε at achievable loading, the real part of the susceptibility must be near its maximum. For a SHO, this means that the imaginary part of the susceptibility is very nearly equal to the real part. It follows that in any metamaterial sample operating in this regime, for every 2π optical phase shift, the intensity, I , due to absorption caused by dissipative ohmic losses, decreases by a factor of e^{-2} . This rules out the possibility of practical 'perfect lenses' [21], however, other useful devices, such as those relying on hyperbolic dispersion, are possible.

Colloidal Nanoparticle Displays

Palffy-Muhoray, Taheri

Through our experimental characterization and theoretical modeling of gold nanorods, we have learned that metallic nanoparticles behave in many ways just like dichroic dye molecules; they show well defined absorption bands and strong dichroism. They differ from dye molecules in two critically important ways:

1. unlike dye molecules, they can be easily oriented by electric fields, and
2. their absorption band can be easily tuned almost anywhere in the visible and IR spectrum by changing their shape.

The first effect is due to their size; since the polarizability is proportional to volume, nanoparticles are large enough that interaction energy with an applied field (of the same magnitude as in LCDs) is greater than kT , large enough to overcome thermal randomization. The second is due to the fact that the frequency of plasmon resonance, which determines the absorption band, is determined by the particle shape; essentially the aspect ratio. These two key features suggest that colloidal nanoparticle suspensions may be well suited for display applications. We have shown, under this MURI, that AuNRs, appropriately stabilized with thiolated surfactants in organic hosts can be oriented with electric fields. We have also subsequently demonstrated that these systems may be used as simple, low-cost, flexible, plastic-based displays. They are similar to liquid crystal guest-host displays, but without the stringent requirements of alignment layers and precise control of cell gap thickness; they can furthermore be easily tailored to operate anywhere in the visible or the IR. These aspects may be useful for the design of a variety of devices, such as those used in night vision applications (near IR and IR based IFF). Because of its potential in addressing warfighter needs, this technology has been transferred to *AlphaMicron, Inc.* where preliminary work is being carried out to determine baseline performance under funding through the Nanostructured and Biological Materials Branch AFRL/RXBN, Wright-Patterson AFB (Richard A. Vaia).

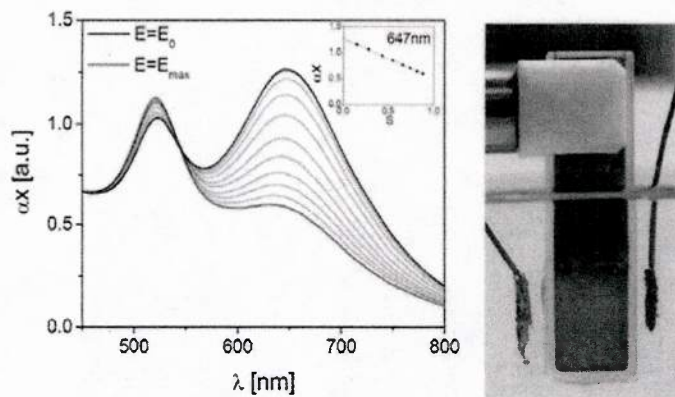


Fig. 22. Absorption spectrum and cell under the influence of an applied E-field.

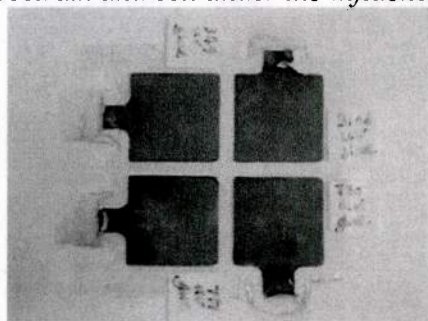


Fig. 23. Flexible 2"x2" near IR AuNP cell developed by in by AlphaMicron.

New York University

PI: Leslie Greengard

During the course of the MURI, the NYU group has concentrated largely on the development of fast algorithms for the evaluation of electromagnetic fields in microstructured materials with complex geometry.

A new method was developed, called FMPS (Fast MultiParticle Scattering), which can be applied to microstructured materials consisting of separated inclusions which are embedded in a homogeneous background [26]. Since, in practice, it is often the case that the shape and permittivity of the inclusions are fixed, the design questions revolve around the optimization of their placement to create a specific electromagnetic response. Each new configuration requires the solution of the full Maxwell equations. If there are thousands of inclusions in an electrically large region (many wavelengths in size), the calculation has historically been too expensive to carry out within a design loop. In order to accelerate such calculations, FMPS couples complex geometry Maxwell solvers with multiple scattering theory. Using the hybrid solver, calculations with million degrees of freedom require only a few minutes on a single CPU.

We developed open source libraries for FMPS and the related fast multipole methods, and made them publically available through the Courant Mathematics and Computing Laboratory website.

Since some scatterers involve multiple material junctions, we developed novel integral equations methods to handle such situations, generalizing the Muller-Rokhlin formalism for dielectric scattering. Fast, high order accurate schemes were shown to be feasible using a new potential-theoretic formalism, fast multipole acceleration, and adaptive mesh refinement on the interface [22]. Since nanorings (tori) are objects of interest in metamaterial synthesis, we investigated and solved a longstanding problem in low frequency scattering - namely the breakdown of the magnetic field integral equation for multiply-connected domains [23]. We studied some basic questions concerning the modeling of quasiperiodic scattering and developed a new approach to the solution of such problems that bypass the use of the quasi-periodic Green's function and enable the use of integral equation methods even when that Green's function fails to exist (at so-called Wood anomalies) [24,25]. Finally, in a series of papers [27,28], we developed a new representation of electromagnetic fields in terms of two ("non-physical") variables - generalizing the Debye representation to surfaces of arbitrary shape.

The effective design on optical metamaterials requires accurate and efficient computation of the optical response. Existing commercial software (such as CST Microwave Studio) is designed to work with periodic structures. Self-assembled metamaterials are typically not periodic. Currently available methods (discrete dipole approximation or finite difference time domain) of dealing with these are neither sufficiently fast or accurate. Greengard's group has developed the fast multiparticle scattering scheme for aperiodic metamaterials; this scheme is now fully functional. Using this, we have recently (Tri-service review, 24/5/10) shown that the response of periodic or random distributions of oriented Au NR pairs is essentially the same, and

that negative index (as calculated from the phase of transmitted light) can indeed be realized not only from NR pairs, but also from assemblies of individual NRs. The code is now ready to be distributed, on both Windows and Linux platforms with Fortran and Matlab interfaces. A screenshot of the program with the Matlab interface is shown above. Because of its efficiency, accuracy and unique ability to deal with aperiodic structures, this software will undoubtedly become an invaluable tool in computational optical metamaterials design.

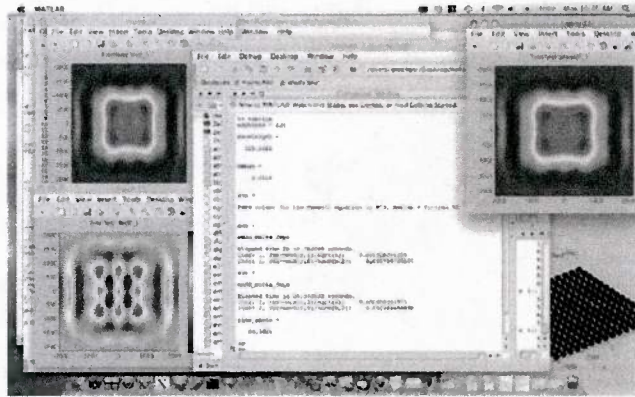


Fig. 24. FMPS code with Matlab front end.

Software:

FMPS: <http://www.cims.nyu.edu/cmcl/fmps/fmps.html>

FMM2D: <http://www.cims.nyu.edu/cmcl/fmm2dlib/fmm2dlib.html>

FMM3D: <http://www.cims.nyu.edu/cmcl/fmm3dlib/fmm3dlib.html>

University of Central Florida

PI: Eric Van Stryland

Characterization of the nonlinear properties of NIMs

CREOL has performed studies of the nonlinear optical properties of metal nanoparticles of differing sizes and shapes to determine the nonlinear absorption spectra and dispersion of nonlinear refraction. These studies cover spectral regions near the plasmon resonance where potential negative index material, NIM, properties are possible. Thus given a NIM material we should be better able to predict their nonlinear optical response.

We have been investigating the nonlinear optical, NLO, properties of nanostructured materials in preparation for performing such studies in negative index materials, NIM's. The initial NLO characterization has been performed on suspensions of metallic nanoparticles in water and other solvents, and thin films of metallic particles in comparison to solid metal films of various surface structures. The suspensions of various sizes and shapes of metal particles have been studied by using our Z-scan technique and by pump-probe techniques using various pulsewidths at different wavelengths. We have capabilities to study NLO responses over 6 orders of magnitude in pulsewidth (from ~ 10 fsec to 10 nsec) and over a very broad spectral range (UV to IR). The following figures show the two primary techniques we have used:

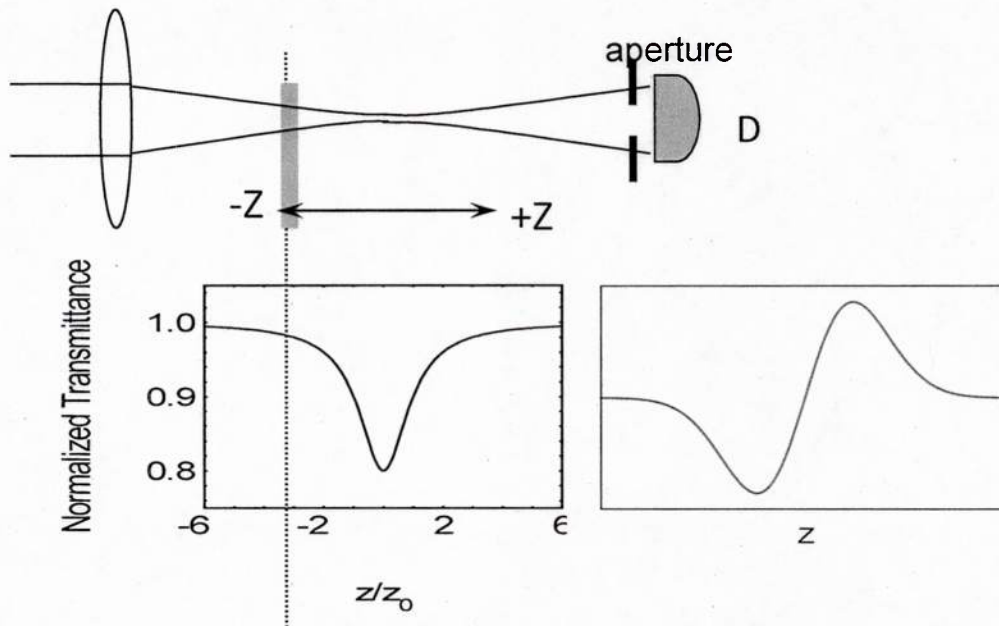


Fig. 25. Z-scan: the sample is scanned along Z and the transmittance of an aperture—either “open” or “closed” placed in the far field is measured. The graphs at the bottom show the results. (reference: ??????)

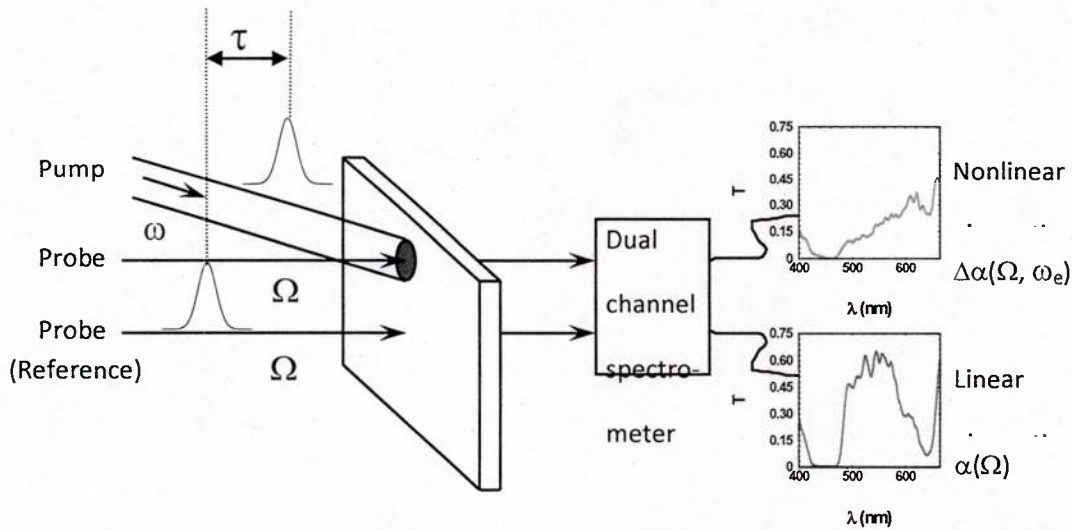


Fig. 26. White light continuum pump-probe technique where a fixed frequency pump changes the nonlinear optical absorption of the sample and the probe (we use a white light continuum for spectroscopic analysis) measures the change in transmittance induced by the pump. (reference, Negres RA, Hales JM, Kobayakov AK, Hagan DJ, Van Stryland EW, "Experiment and Analysis of Two-Photon Absorption Spectroscopy Using a White-Light Continuum Probe", IEEE JOE 38 (9), 1205-1216 (2002).

Fig. 25 shows results of Z-scans showing nonlinear absorption and nonlinear refraction. If these occur simultaneously, the effects can easily be separated by dividing the results of the closed aperture Z-scan by those from the open aperture Z-scan. The source of the Z-scan can be directly from a laser or optical parametric source or filtered light from a White-Light Continuum, WLC. Using the WLC allows rapid extraction of the spectrum of nonlinear absorption along with the dispersion of the nonlinear refraction [34, 35].

While the Z-scan gives the frequency degenerate nonlinearities, Fig. 26 shows a femtosecond pump- WLC probe method we developed for measuring the nondegenerate nonlinearities. Here the nonlinear refraction can be related to the nonlinear absorption spectrum via nonlinear Kramers-Kronig relations.

The following gives a summary of our most important findings. Periodic reports with greater detail are on the NIM MURI web page.

We worked with researchers at Kent State who developed a method for aligning metal nanorods to measure their NLO properties. Fig.27 shows the linear absorption spectra of such rods in various fields showing various levels of orientation.

Nanorod 724

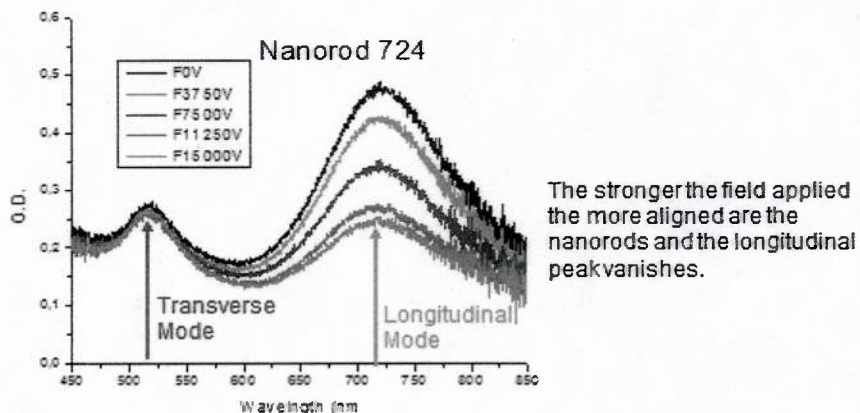
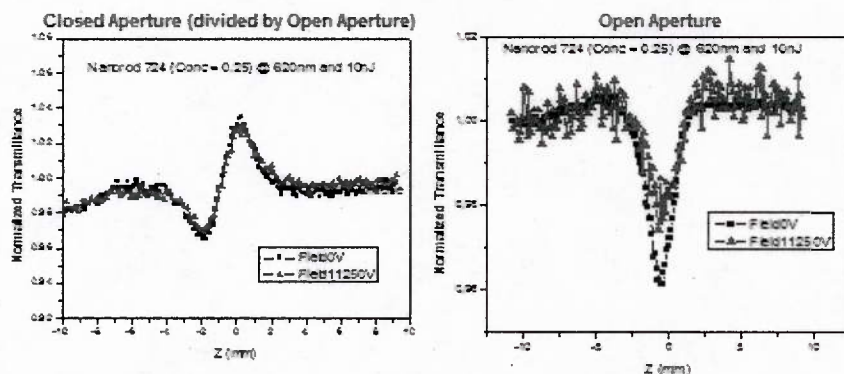


Fig. 27. Metal nanorod suspension linear absorption spectra in various electric fields.

@ 620nm...



Alignment of the nanorods does not cause a big change on the nonlinear refraction, but only on the nonlinear absorption, which decreases, since the linear absorption also decreases.

On the open aperture Z-scan we see a positive effect (increasing on the absorption)

Fig. 28. Z-scan measurements of suspensions with and without an aligning electric field.

Researchers at GeorgiaTech (Bernard Kippelen et al) sent us sample of metallic thin films having different thicknesses and surface roughness. The thinnest and therefore the roughest showed metallic islands as opposed to a continuous thin film and qualitatively different optical properties. Fig. 29 shows micrographs of the surfaces. Fig. 30 shows open aperture Z-scans.

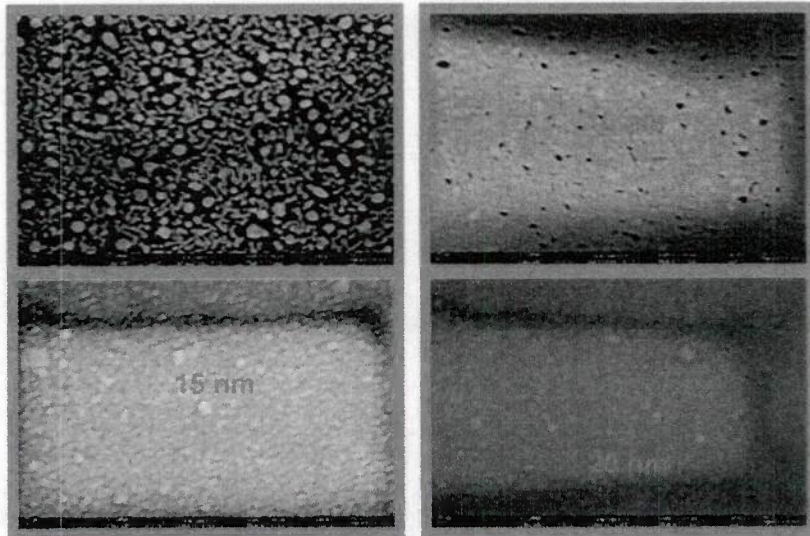


Fig 29. Micrographs of the metal films produced by GeorgiaTech.

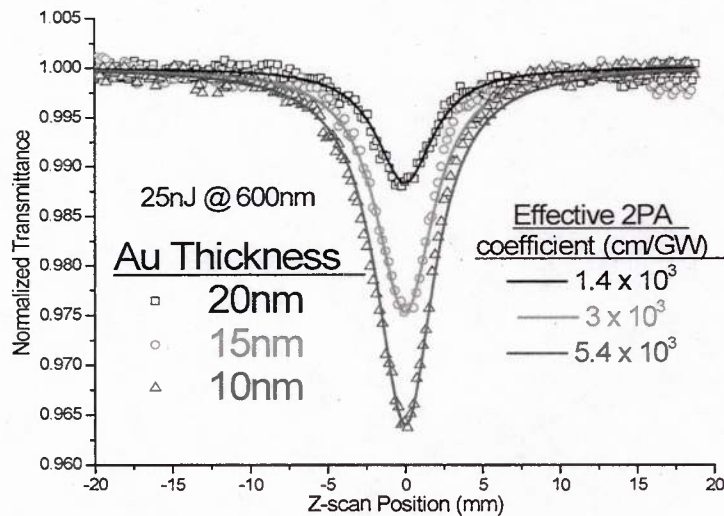


Fig. 30. Open aperture Z-scans of 3 of the metal films produced by GeorgiaTech.

The results of measurements of the nonlinear absorption show a decreasing nonlinear response with increasing thickness. The increased nonlinear absorption is due to the increased field inside the thinner samples where reflection from the back surface is important and is not due to a difference in the metal response. The thinnest film is not a continuous film of metal so that it shows a very different nonlinear response and plasmon resonances. We also looked at several other samples provided by multiple research groups including Wake Forrest. Below we show some interesting results on field enhancement with the metal rods to enhance the nonlinearity of organic dyes in close proximity to the metal.

Nonlinear enhancement capabilities

There have been several studies where people reported large increases in the nonlinear properties of materials in close proximity to metal nanoparticles. This could be important for several nonlinear optical device applications so we attempted to see this field enhancement in nonlinear absorption.

When embedded in a host material which exhibits an intrinsic nonlinearity such as two-photon absorption, the strongly confined, high electric fields around the nanostructures should enhance the material's optical nonlinearity relative to its intrinsic value. This was examined using silver nanoparticles in carbon disulfide. The carbon disulfide two-photon absorption band spectrally coincides with the plasmon resonance of silver nanospheres where the highest enhancement is found.

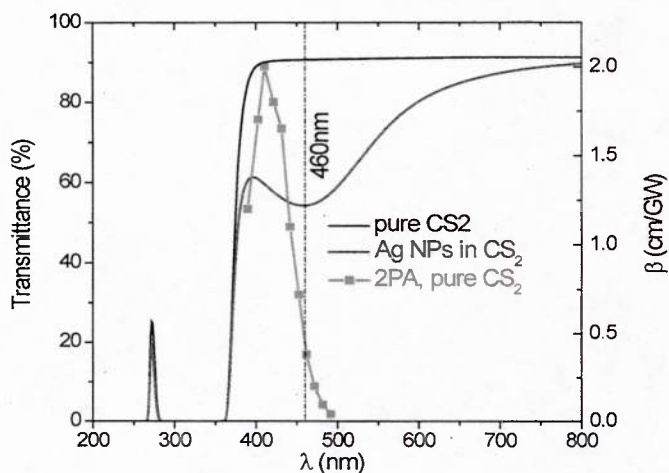


Fig. 31. Linear and 2PA spectra of pure carbon disulfide, CS_2 and 15nm Ag nanospheres in CS_2

Z-Scan experiments of a silver nanospheres- carbon disulfide colloid were conducted and gave a combined signal of two-photon absorption and saturable absorption associated with the broadening of the plasmon band. See Fig. 32 and linear spectra in Fig. 31.

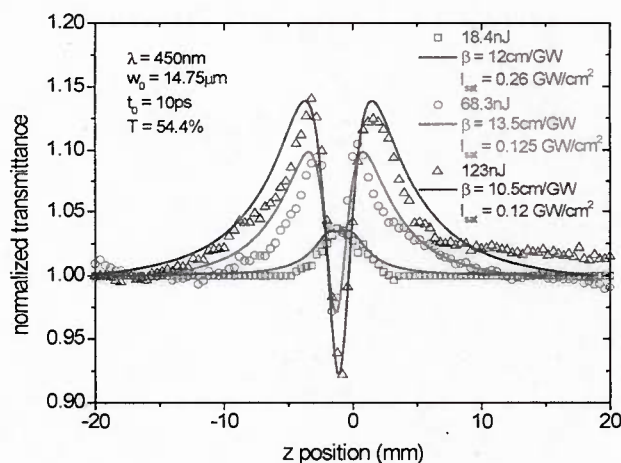


Fig. 32. Z-Scan data of silver nanospheres –CS₂ colloid.

Using a two level homogeneously broadened saturation model, $\alpha(I) = \alpha_0/(1 + I/I_{sat})$, revealed a two-photon absorption coefficient of $\beta = 12 \text{ cm/GW}$, which constitutes an 4.7-fold enhancement, i.e., the average two-photon absorption of $\beta = 12 \text{ cm/GW}$ is 4.7 times higher than in pure carbon disulfide at this wavelength. Pursuing this further we studied a two-photon absorbing dye in solution with and without metal nanoparticles present.

Fig. 33 shows a Z-scan of a sample of a Hoeschst dye (shown in the figure) after metallic nanoparticles were added and NaCl was added to cause some agglomeration of the particles.

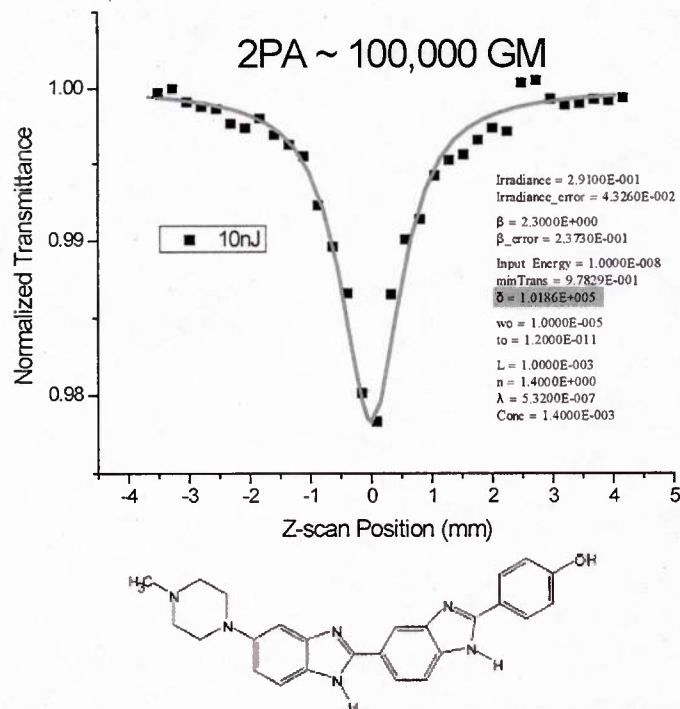


Fig. 33. Z-scan of the dye (shown on the right) in solution with metal nanoparticles and salt solution after 1/2 hour.

Approximately one-half hour after NaCl is added to the solution of dye and with the suspended nanoparticles, the particle agglomerate in such a way that the field is enhanced as evidenced by the increasing Z-scan signal. Unfortunately this process is very irreproducible, and it took many tries to get this data. In addition, about 20 minutes after this data was taken the metal precipitates out and the enhancement is lost. The observed enhancement at its peak is about 40 times larger than the dye solution without metal and salt. {dye solution by itself: 2PA average $\alpha_2 = (9 \pm 0.2) \times 10^{-11} \text{ cm}^2 \text{ W}^{-1}$, 2PA effective $\sigma_2' = 2,400 \times 10^{-50} \text{ cm}^4 \text{ s photon}^{-1} = 2,400 \text{ GM}$ } {Dye + Au + NaCl in solution: 2PA effective $\sigma_2' = 100,000 \text{ GM}$ }. This is actually considerably lower than the enhancement reported in the literature, so we suspect that given proper sample preparation we could have observed a greater enhancement. But it is as yet unclear if this enhancement can somehow be stabilized for long-term use. This might be done by using a photopolymerizable solvent. Further research in this area should be pursued.

We also looked at 2-dimensional lattices of metal nanoparticles produced by optical lithography. Two different groups sent us samples. The group of Shalaev at Purdue and the group of Martin Wegener in Karlsruhe, Germany. One of our graduate students, Oliver Kahl, meets with him in Germany relatively frequently and has helped in sample preparation there. Below we give the latest results for the samples from Karlsruhe. Fig. 34 shows SEM images of two of the samples we studied.

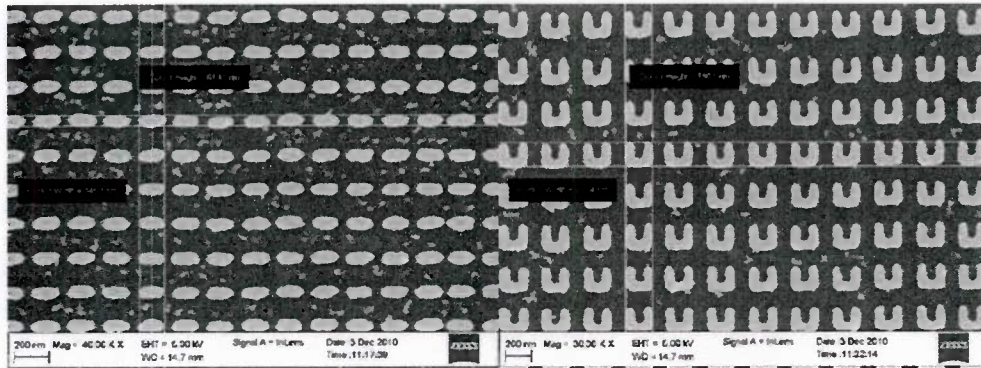


Fig.34. SEM image of gold NRs on glass, left, rod shaped nanoparticles on glass; right, gold split ring resonators on glass.

Nonlinear properties of Karlsruhe samples

The absorption of photons by the free electron gas leads to a temperature increase of, firstly, the free electrons themselves, followed by an equilibration with the lattice which raises the lattice temperature. The transient temperature change of the electron gas, which can briefly reach several thousand Kelvin, is reflected in a change in the dielectric function, which, in turn, determines the optical properties of the material. Some of the explanations below describe experiments on other samples as well.

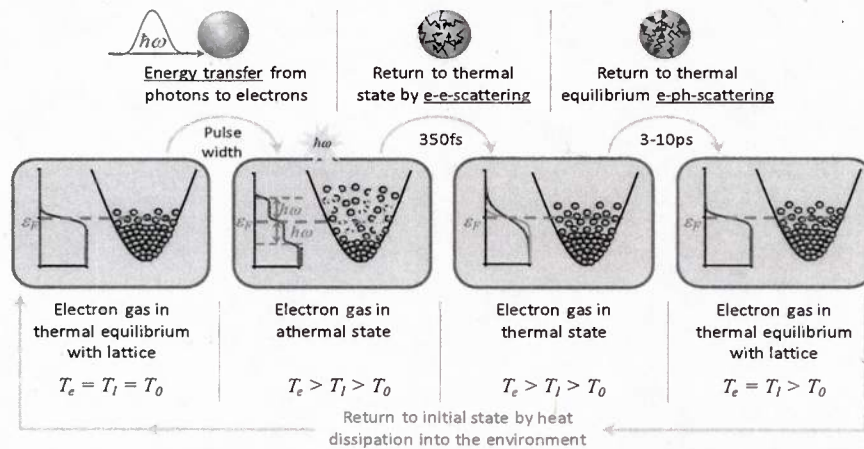


Fig. 36 Pictorial explanation of the two-temperature model.

Fig. 36 gives a summary of the two temperature model for explaining the response of metals. A plot of the temperature as a function of time for the electrons and lattice is presented in Fig. 37.

The dielectric function of gold includes contributions from d-band to s-p-band transitions around the L- and the X-point at 2.35eV and 1.94eV, respectively. These contributions can, however, be avoided by choosing sufficiently low photon energies, which allows for a Drude-type metal treatment. Pump-probe experiments in this regime showed a broadening of the

longitudinal plasmon resonance of gold nanorods, when pumped at the resonance wavelength as shown in Fig. 38.

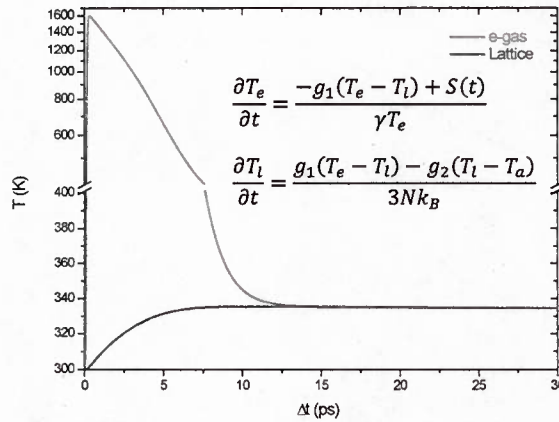


Fig. 37. Calculation of the temperatures in the two-temperature model described in Fig. 37

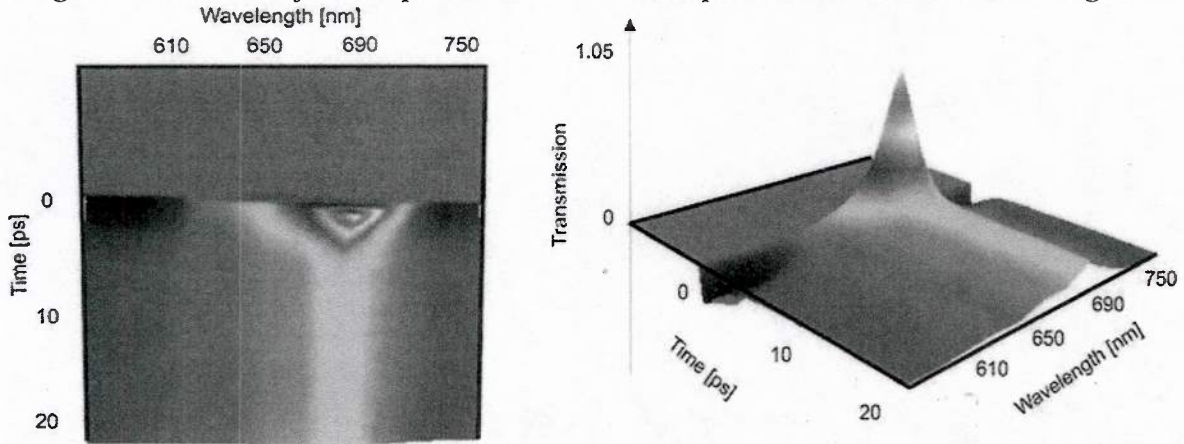


Fig. 38. Transient transmission spectra of the longitudinal plasmon resonance of gold nanorods on glass at 690nm reveal a broadening of the resonance upon strong irradiation

The same experiment with a split ring resonator sample showed an additional phenomenon: rapid heating causes thermal expansion. If the heating occurs on timescales as short as a few picoseconds, the material tends to expand beyond its equilibrium point leading to a subsequent contraction and eventually to a damped oscillation in the structure size. These so called acoustic modes can be seen in pertinent pump-probe data, as the spectral position, which inherently depends on the structural geometry, shifts with changes in the geometry such as expansion and contraction:

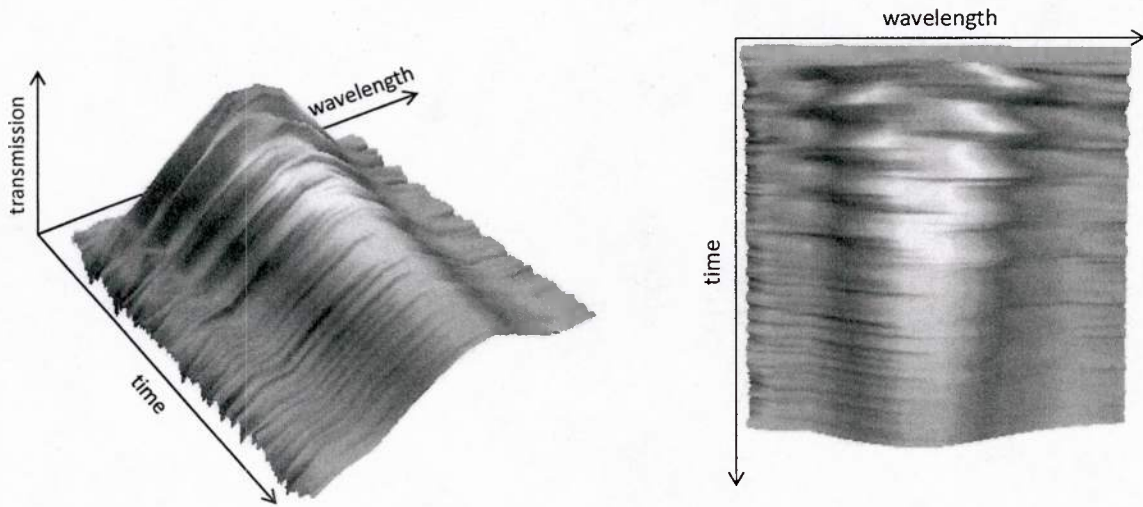


Fig. 39. Transient transmission spectra of Au split ring resonators at the fundamental magnetic resonance around 1500nm reveal periodic blue and red shifts associated with acoustic modes in those structures

By fitting the Lorentzian shaped absorption features to the obtained data, the changes in the Drude damping parameter Γ and the center frequency ω_0 are found. As can be seen in the following Figures 40, 41, these parameters change by about the same amount.

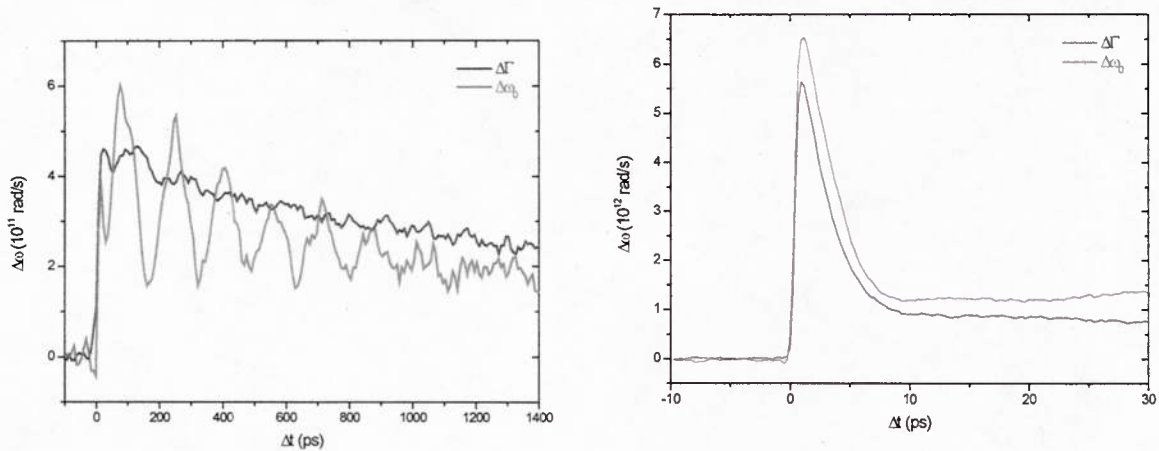


Fig. 40. Temporal evolution of the center plasmon frequency and the Drude-type damping factor: Left: gold split ring resonator on glass; right: gold nanorods on glass

Using the data obtained, it is possible to correlate the Drude damping term to the electron gas and lattice temperatures. Fitting the data to a function of the form $\Gamma(T_l, T_e) = A + BT_l + CT_e^2$, the following coefficient values are obtained for the gold nanorods on glass: $A = 2.1214 \times 10^{14} \text{ s}^{-1}$, $B = 2.8703 \times 10^{10} \text{ s}^{-1}\text{K}^{-1}$, $C = 2.8271 \times 10^7 \text{ s}^{-1}\text{K}^{-2}$.

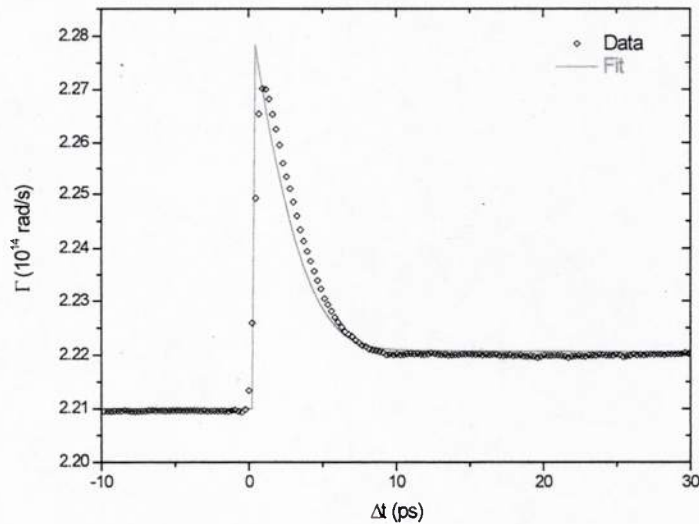


Fig. 41. Averaged data for damping changes of gold nanorods on glass including fit obtained by utilizing above fitting formula

Linear properties

Metallic nanostructures exhibit strong, polarization dependent absorption and scattering resonances due to the confinement of radiatively excitable free electrons. The spectral position of these features depends strongly on the geometry of the structure: Spheres show one single resonance, rods two (transvers + longitudinal), more complex geometries (e.g. split ring resonators) can possess many more.

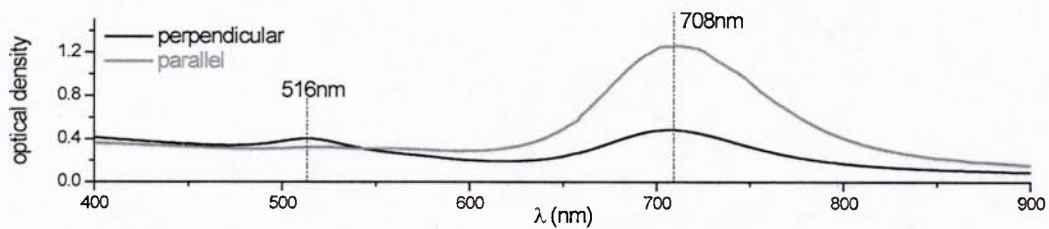


Fig. 42. Absorption spectrum of gold nanorods in polyurethane (stretched 10x its original length) showing a transverse and longitudinal absorption peak at 516 nm and 708 nm, respectively.

University of California at San Diego

PI: Sheldon Schultz

Near-field Interaction of Self-assembled Au Nanorod Negative Index Materials (NIMs)

Introduction

The primary focus of this research was to develop negative index materials (NIMs) at the nanoscale, where the negative index of refraction results from negative permittivity ($\epsilon < 0$) and permeability ($\mu < 0$) in the VIS-IR wavelength range. Since the discovery of NIMs by our group in 2000 [29], it was evident that sub-wavelength structures comprised of metal nanoparticles exhibited great potential at optical frequencies as nanoscale NIMs.

To understand the electromagnetic response of nanostructures it was essential to first examine single nanoparticles and then progress to self-assembled nanoscale structures. In order to obtain meaningful results systematic changes in surface functionalization, inter-particle spacing, and geometrical structure were examined optically using polarized light spectroscopy. The nanoscale base units used in the experiments were Au nanorods due to their excellent electromagnetic properties. Monodisperse solutions of single nanorods and self-assembled structures having PEG/CTAB and polymeric shells were fabricated within our division of the AFOSR program and also custom shelled by Nanopartz Corporation.

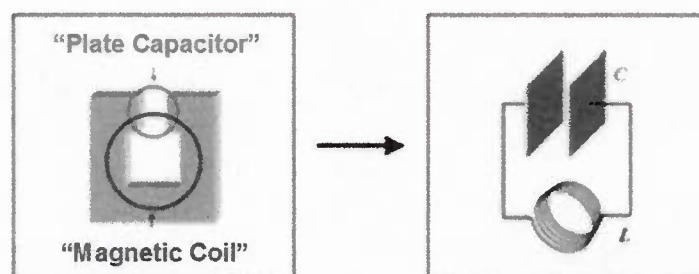


Fig. 44. Split-ring resonator acts as LC-oscillator for specific incident light frequencies.

In order to obtain a magnetic response from the metal nanostructures an incident light field has to excite local currents circulating in loops (solenoidal currents), thus resulting in a magnetic dipole moment. Proper nanostructure design can result in the enhancement of local currents thus leading to negative magnetic permeability. The nanostructure thus acts like a sub-wavelength split-ring resonator (SRR) as in Fig. 44 consisting of a magnetic coil with inductance L and capacitor with capacitance C . An array of these nanostructures will result in a so-called metamaterial. Theoretical calculations have shown incident light for frequencies just above the LC-resonance can result in negative effective permeability.

Fabrication of basic nanoscale SRRs using non-lithographic techniques is challenging with the simplest structure predicted to exhibit this type of response being pairs of closely spaced

nanorods. The research presented here focused on developing an optical imaging system to examine shifts in spectral response of nanorods due to dielectric shells $\epsilon_{\text{shell}}(\omega)$ and the effects of near-field electromagnetic interaction of nanostructures using angularly resolved polarized light spectroscopy.

Experimental Setup

To examine optical properties of individual nanorods and nanoscale NIM structures a special system was designed using precision translational (XYZ) and rotational (θ) stages to control the exact position (orientation) of the plasmon resonant nanoparticles (PRNPs) with respect to the optical axis of the microscope objective in Fig. 45. The present design has translational accuracy of $\Delta = 50$ nm in all directions with angular resolution enabling measurement intervals of $\Delta\theta = 0.5^\circ$. A special alignment post has been fitted to hold and orient scanning electron microscope (SEM) posts having silicon wafers as the substrate to immobilize particle samples. This technique removes ambiguity of reference orientation plus enables SEM mapping of surface region of interest for comparison with the darkfield field of view seen optically.

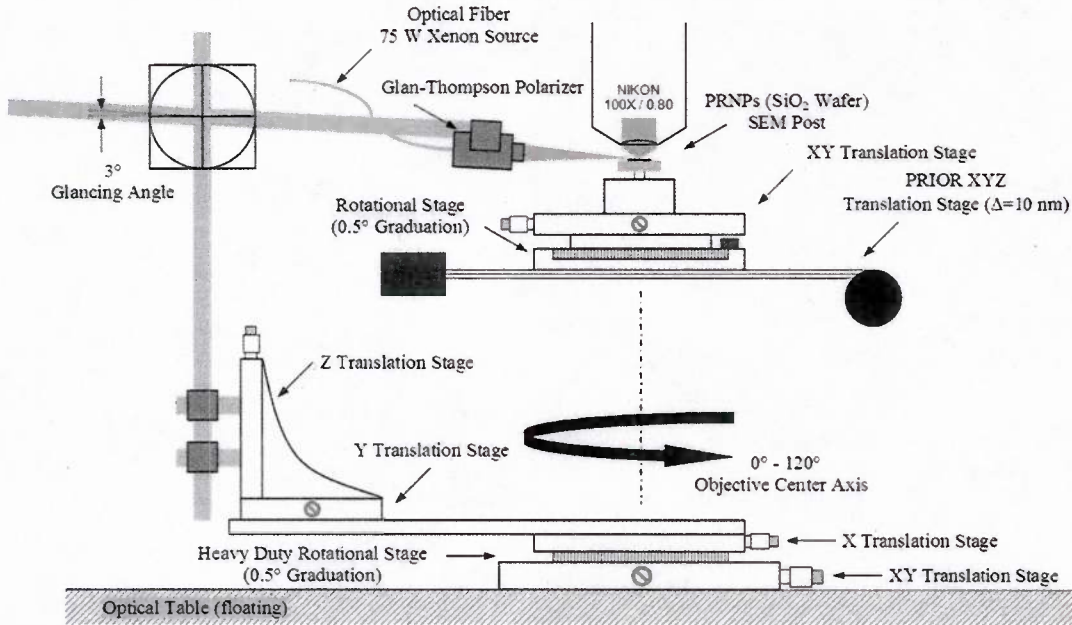


Fig. 45. Polarized light rotation assembly for single nanoparticle spectroscopy. Light source has precise translational and rotational movement about the microscope objective optical axis.

In Fig. 45 the 75W Xe light source is focused using the numerical aperture (NA) of the fiber and passed through a polarizer before being focused onto a 2 mm spot at 3° glancing angle on a SiO_2 substrate. Polarized light is rotated about the objective axis through 120° thus enabling examination of optical changes due to electromagnetic effects as a function of angle.

Improvements in illumination using high transmission optical fibers has resulted in increased intensity and control of electric field polarization with respect to the imaging surface using a Glan-Thompson polarizer with the highest optical grade calcite. This has improved signal to noise ratio (SNR) and resulted in highly resolved spectra.

Polarized Light Spectroscopy

A Nikon microscope with CF Plan BD 100X (NA/0.8) objective as shown in Fig. 45 is used to obtain resonant scattered light spectrums from individual nanorod structures. The scattered light within the acceptance cone of the objective is guided through a 2X relay to an image plane aperture (0.2 mm) to reduce stray light contributions from nearby regions by centering the point spread function (PSF) within this aperture. Light is redirected from the aperture into an SPEX 270M spectrometer having dual gratings with 35 nm and 220 nm spectral windows using a mirror and focusing lenses. Individual spectra are captured using a Princeton Instruments model 1300YHS cooled CCD camera (1300 x 1030, 5 MHz Interline) to record light intensity (vertical pixels) as a function of the wavelength across the CCD (horizontal pixels). Spectra are background subtracted and normalized to the light source using the spectrum obtained off the surface of a perfect white reflectance standard.

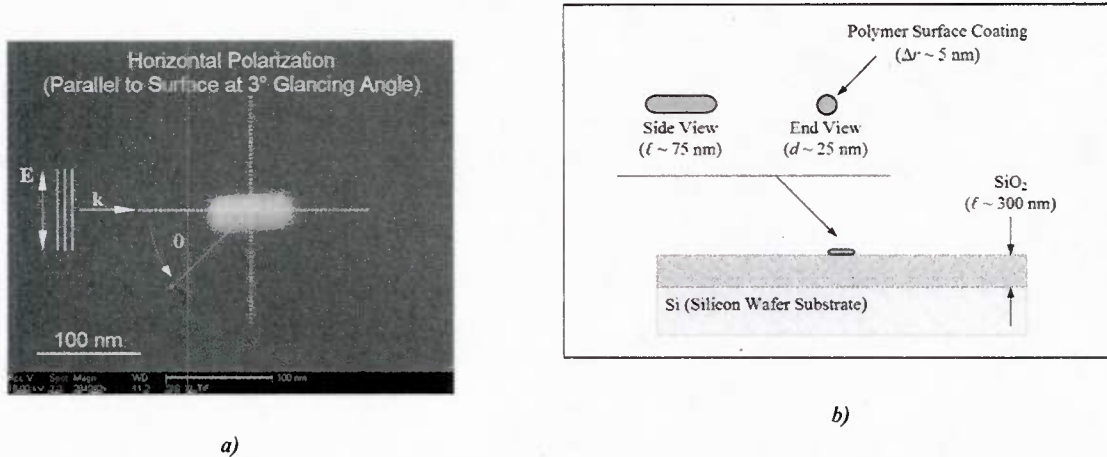


Fig. 46. (a) Overlay of polarized light angular (θ) position on SEM image of single (25 nm x 75 nm) Au nanorod. (b) Substrate schematic indicates the SiO_2 thermal oxide layer on which PRNP is lying.

It was found previously within our group that silicon wafers are an excellent imaging surface but it requires a thermal oxide layer of about $\ell \sim 300$ nm as shown in Fig. 46(b) to avoid formation of an image charge which attenuates the electromagnetic response. The polarized light is incident at 3° glancing angle to the silicon surface as in Fig. 46(a) with the electric field polarized parallel to the surface and perpendicular to direction of wave propagation. This configuration has enabled us to accurately examine the strength of the electromagnetic response and peak shift to longer wavelengths as the angle (θ) increases between the electric field and

nanorod axis. Optical properties of the substrate in Fig. 46(b) plus dielectric shell have also been taken into account in modeling calculations.

Individual nanostructures are sub-wavelength so a mapping technique was developed using sequentially lower magnification SEM images to provide fiduciary reference points plus establish orientation and relative position with respect to precision scribe lines. This type of mapping enabled us to examine regions of interest in optical darkfield images at 100X magnification and center potential NIM nanostructures on the optical axis. Although it was possible to spin a single nanorod about its center, uncertainties in the runout of the rotational stage were avoided through polarized light rotation shown in Fig. 44.

Experimental Results

Self-assembled nanostructures having potential NIM characteristics and monodisperse nanorod (Au, Ag) solutions were fabricated and post processed to achieve special surface functionalization. Shelled nanorod surface chemistry is critical in preventing irreversible aggregation and controlled formation of specific nanostructure configurations. Nanorod aspect ratios were fixed at 1:3 for all particle suspensions to enable comparison of results with other divisions within the AFOSR NIMs program.

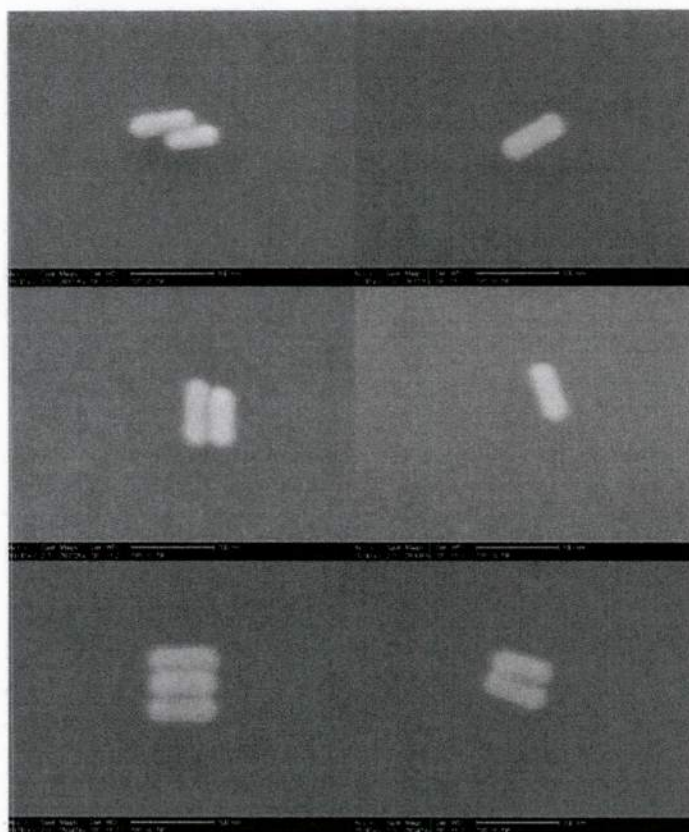


Fig. 48. SEM images of single and self-assembled Au nanorods that are surface functionalized with 5 nm polymeric (PEG) dielectric shells.

Through systematic tests it was found that control of the particle concentrations and CTAB/pH levels resulted in the formation of self-assembled nanostructures as shown in the SEM images in Fig. 48. Since the polymeric (PEG) shell is acting only as the dielectric insulator between rods, the electromagnetic effects were minimized by keeping the shell thickness at 5 nm. Optical investigation of the coating using ellipsometric light scattering verified that the shell is lossless with $\epsilon = 2$ for visible light frequencies. Since the optical constants for Au and SiO₂ are in general complex and frequency dependent the published values were used in assessing our results and in simulation models. Interparticle spacing seemed to be affected by the solutions pH and needs to be explored further to understand near-field coupling as the distance of separation is increased.

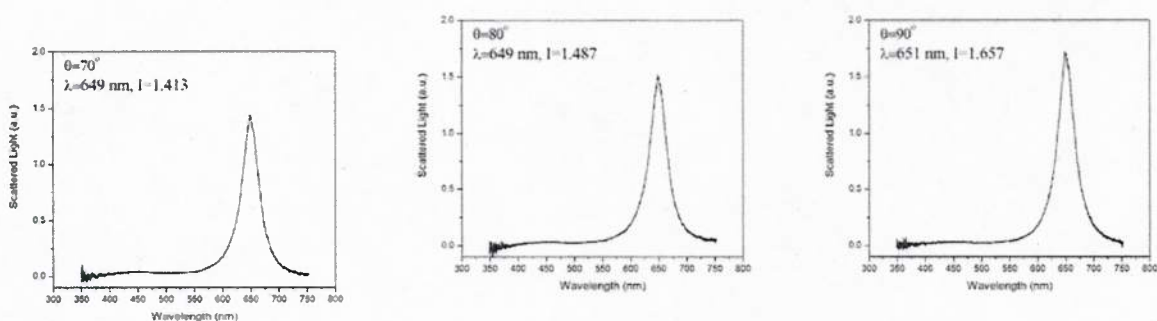
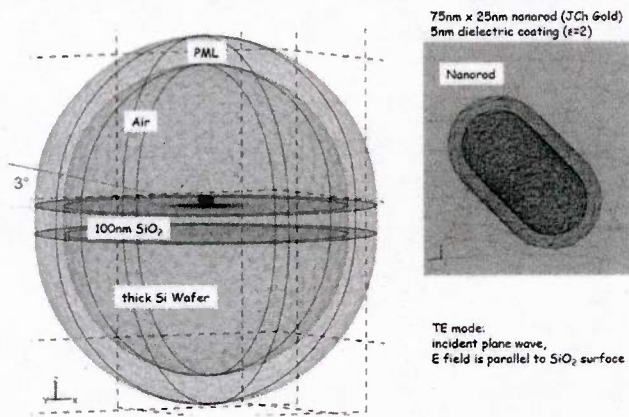


Fig. 49. Optical spectra for horizontally polarized light incident on a single Au nanorod on the SiO₂ layer as in Fig. 46(a) as the light is rotated from 70° to 90° with respect to the nanorod axis.

The spectroscopic imaging system in Fig. 45 has enabled us to examine the changes in optical spectra for single Au nanorods due to variations in length and the relative angle of the electric field with respect to the nanorod axis. In Fig. 48 an increase in scattered light intensity and slight shift of peak wavelength for the nanorod in Fig. 46(a) is shown as the relative angle is changed. These spectra indicate the tremendous resolution and sensitivity of our system, which is essential in examining potential nanoscale NIM structures.

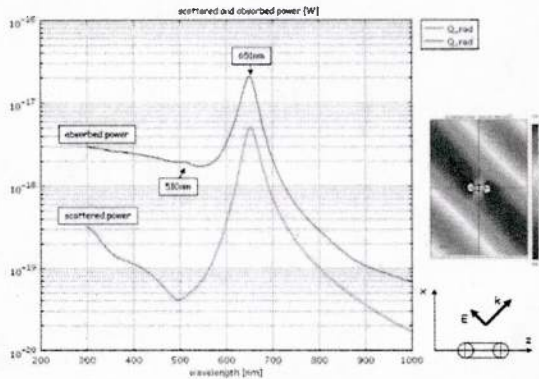
Nanostructures composed of self-assembled parallel Au nanorods were examined and compared as shown in Fig. 49. The center to center separation of nanorods is 40 nm, with the respective dielectric shells physically separated by a 5 nm gap, thus metal surfaces are separated by 15 nm. Incident polarized light was fixed at 90° with the electric field along the long axis of the nanorods. As evidenced in the experimental spectra the scattered light intensity increases due to near-field electromagnetic coupling. There is roughly an 18% increase in amplitude between a single Au nanorod (25 nm x 75 nm) and three equivalent nanorods forming the self-assembled nanostructure in Fig. 49. The near-field interaction of individual resonances also resulted in peak wavelengths being blue-shifted. In Fig. 49 the peak location has blue-shifted by ~ 18 nm for the nanorod pair and ~ 40 nm for the triplet relative to the single nanorod spectrum.

Simulation geometry for "foreground" problem: comparison 300nm vs. 100nm SiO₂



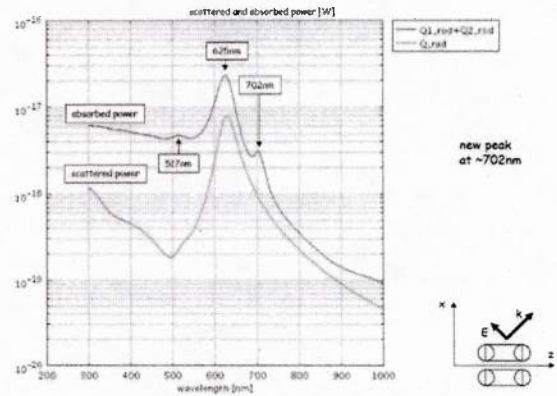
a)

Gold nanorod 75nm x 25nm (35nm w/coating) in z-direction, coated with $\epsilon=2$, lossless; interpolated JCh permittivity, oblique incidence 45deg, $k=(1\ 0\ 1)$; TE mode, $E=(-1\ 0\ 1)$



b)

Pair of identical Gold nanorods in zx plane, 75nm(x) x 25nm(x), 5nm coating with $\epsilon=2$, 40nm(x) separation interpolated JCh permittivity, oblique incidence 45deg, $k=(1\ 0\ 1)$; TE mode, $E=(-1\ 0\ 1)$, vacuum background



c)

Fig. 50. (a) Simulation geometry is based on actual experimental setup for Au nanorods with 5 nm PEG shell immobilized on the silicon wafer oxide layer. (b) The frequency dependent scattered and absorbed power of a single Au nanorod for oblique electric field incidence. (c) Scattered and absorbed power using same simulation geometry for Au nanorod pairs with same oblique incident angle. (Simulation results provided by AFOSR colleague Dr. Thomas Koschny, et al.)

Summary

The current focus of the research is aimed at quantifying blue-shift variations and the enhanced resonance intensity as the nanorod gap size is changed. Advances in the surface

functionalization techniques are also being investigated to control gap spacing in the 5-25 nm range. There is an indication that it may be possible to produce suspensions of self-assembled equilateral triangles composed of three Au nanorods. If this process does work it would provide the first 2-D fluid of nanoscale SRR structures, the first step towards realizing the desired tetrahedral structure that is theoretically envisioned.

A paper on this work is currently being written and is anticipated to be submitted for publication within the next 7 months after more results are obtained. This publication will emphasize our novel setup and unique findings which will benefit the overall progress of the AFOSR NIMs program. In the future we would like to achieve complete experimental agreement with simulation results for any type of nanorod structure and thus formulate a cyclical technique to determine the optimal nanoscale SRR design at optical frequencies.

University of California at San Diego

PI: Sia Nemat-Nasser

3-D Microwave Materials/Models

Microstructurally-based Homogenization of Electromagnetic Properties of Periodic Media

Alireza V. Amirkhizi and Sia Nemat-Nasser

In this work, we have developed a new model to homogenize the electromagnetic properties of a composite with a periodic microstructure, where the length scale of heterogeneity within each unit cell is suitably small relative to the dimensions of the cell and the dimension of the cell in turn is much smaller than the macroscopic size of the body as well as the length of any considered impinging electromagnetic wave. We have used the size of the periodic unit cell as our heterogeneity length scale and have sought to systematically define the constitutive parameters of an equivalent homogeneous body that macroscopically has the same overall response to suitably long wave-length electromagnetic waves. These parameters are the complex-valued effective electric permittivity and magnetic permeability tensors. Unlike the classical approach which requires the solution of the full-field problem and is restricted to a specific wave propagation direction relative to the cells, we have developed a general method based on the volume average of electromagnetic fields that lends itself to a direct evaluation of the overall constitutive electric and magnetic tensorial quantities that are complex-valued function of the wave frequency, ω , and the wave vector, \mathbf{k} . Moreover, our method yields the full 3-dimensional material properties for any wave propagation within the effective-medium limits. Numerical examples have shown the effectiveness of the approach for the dielectric properties. This is a powerful homogenization technique with strong mathematical backing.

Soft Focusing Via Indefinite Anisotropic Dispersion

Sara Wheeland, Alireza V. Amirkhizi, and Sia Nemat-Nasser

The CEAM group has designed and fabricated an anisotropic indefinite composite in microwave regime. The value of permittivity is negative along a structural axis and positive normal to that. We fabricated a 147 mm thick and 220 mm wide Styrofoam sample with an embedded array of 12-gauge brass wires of 6.35 mm lattice spacing. Two single-loop antennas were used to approximately generate a transverse magnetic (TM) point source and the associated detector. Using an Agilent 8510C Vector Network Analyzer (VNA) and a 3D scanner, the frequency spectrum was swept between 7 and 9 GHz in front of the sample in a large rectangular cubic region to locate and measure the relative strength of the focal spot. We established soft focusing spots for source positions at different distances from the sample. These results exhibit the possibility of focusing via negative refraction in hyperbolic indefinite media. The test setup used for measuring the focal spot and representative results indicating a soft spot (on the right)

are shown in Fig. 51 and 52. Note that the focal spot disappears or moves to a different location at other frequencies, since the aspect ratio of the hyperbolic iso frequency curves is strongly frequency dependent.

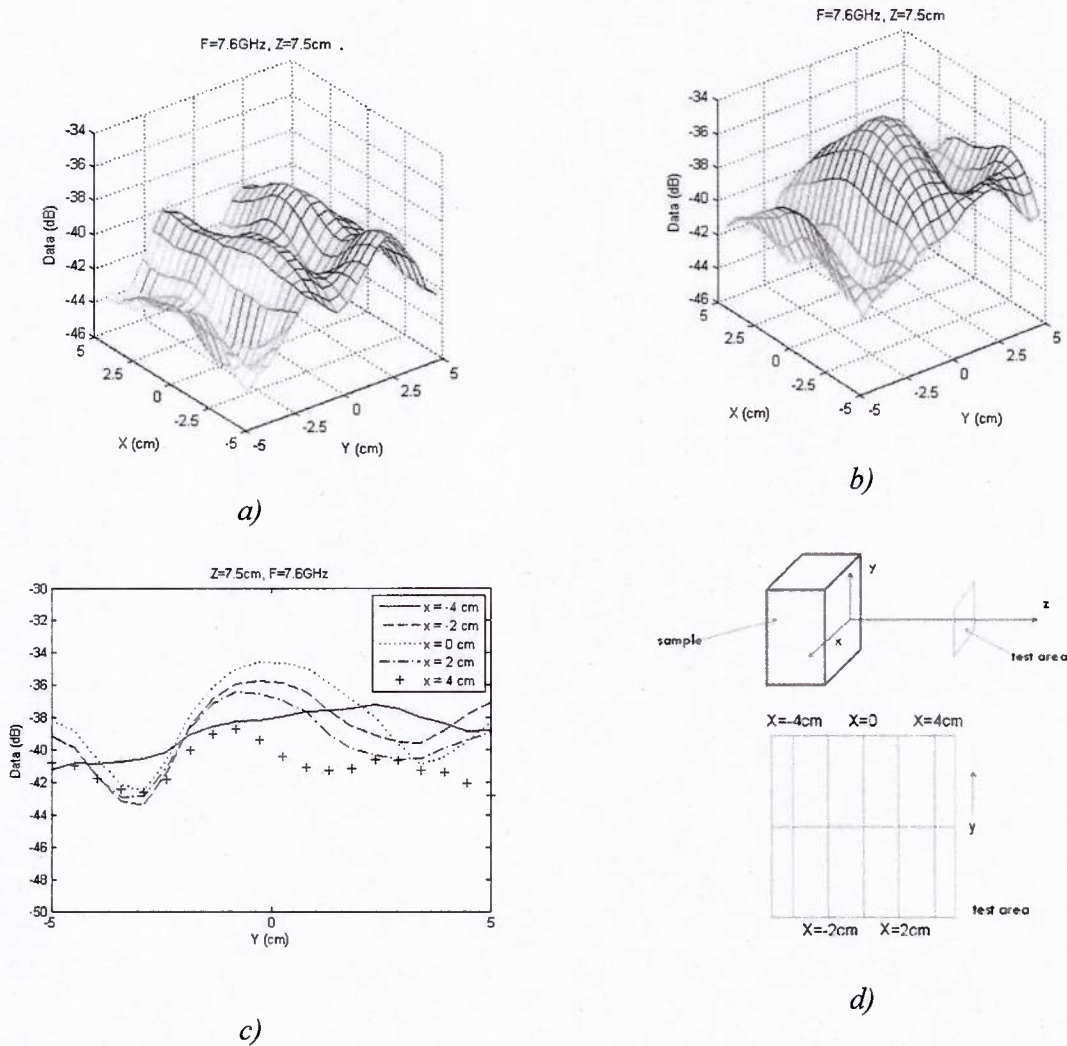


Fig. 51: Transmitter antenna at 7.35cm distance. a) Transmitted power as a function of X and Y at Z=7.5cm (from sample surface) and F=7.6GHz without the sample; b) transmitted power as a function of X and Y at Z=7.5cm (from sample surface) and F=7.6GHz with the sample; c) transmitted power as a function of Y at Z=7.5cm and F=7.6GHz at various values of X; d) schematics of the test configuration.

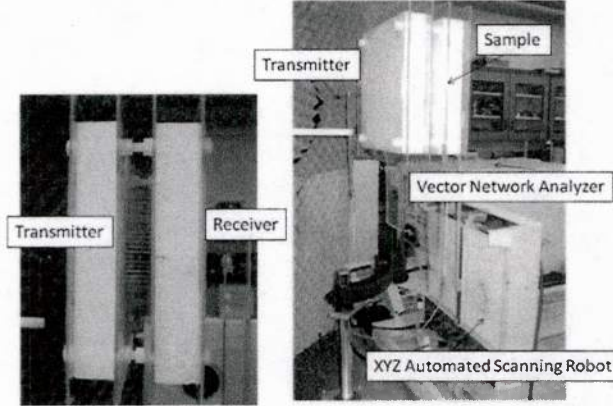


Fig. 52: Test setup showing placement of two point source antennas around the sample with the scanning robot and VNA.

Chiral, Uniaxial, Bianisotropic Media: Analysis and Characterization

Farhad Bayatpur, Alireza V. Amirkhizi and Sia Nemat-Nasser

Artificial bianisotropic media introduce a number of potential opportunities in research on EM metamaterials such as (1) Utilizing the extra degrees of freedom in material properties, i.e. coupling tensors, to achieve negative refraction; and (2) Affecting the left- and right-polarized waves independently. We have focused on design, fabrication, characterization, and analysis of uniaxial chiral media. We have developed a new semi-analytical method for retrieving the constitutive parameters of the materials of this type. An estimate, analytical method provides the initial values, which are then used in a numerical iterative algorithm to find the correct values of chirality, permittivity, and permeability both parallel and normal to the optical axis of the composite.

We have designed a sample with strong uniaxial chiral behavior. The microstructure of this sample consists of an array of helices of similar handed-ness. The fabricated sample and its extracted constitutive parameters are shown in Fig. 53. The notation used in this figure is based on the linear constitutive bianisotropic convention:

$$\begin{cases} \mathbf{D} = \boldsymbol{\varepsilon}\mathbf{E} + \boldsymbol{\xi}\mathbf{H} \\ \mathbf{B} = \boldsymbol{\zeta}\mathbf{E} + \boldsymbol{\mu}\mathbf{H} \end{cases}; \boldsymbol{\varepsilon} = \begin{pmatrix} \varepsilon_{\perp} & 0 & 0 \\ 0 & \varepsilon_{\perp} & 0 \\ 0 & 0 & \varepsilon_{\parallel} \end{pmatrix}; \boldsymbol{\mu} = \begin{pmatrix} \mu_{\perp} & 0 & 0 \\ 0 & \mu_{\perp} & 0 \\ 0 & 0 & \mu_{\parallel} \end{pmatrix}; \boldsymbol{\xi} = -\boldsymbol{\zeta} = \begin{pmatrix} 0 & 0 & 0 \\ 0 & 0 & 0 \\ 0 & 0 & \xi \end{pmatrix}$$

The method has been proven very robust and can easily measure the small changes due to strain of elastic samples. It has been shown that the chirality parameter may be tuned by over 10% in a very wide band of frequency using only around 30% recoverable strain.

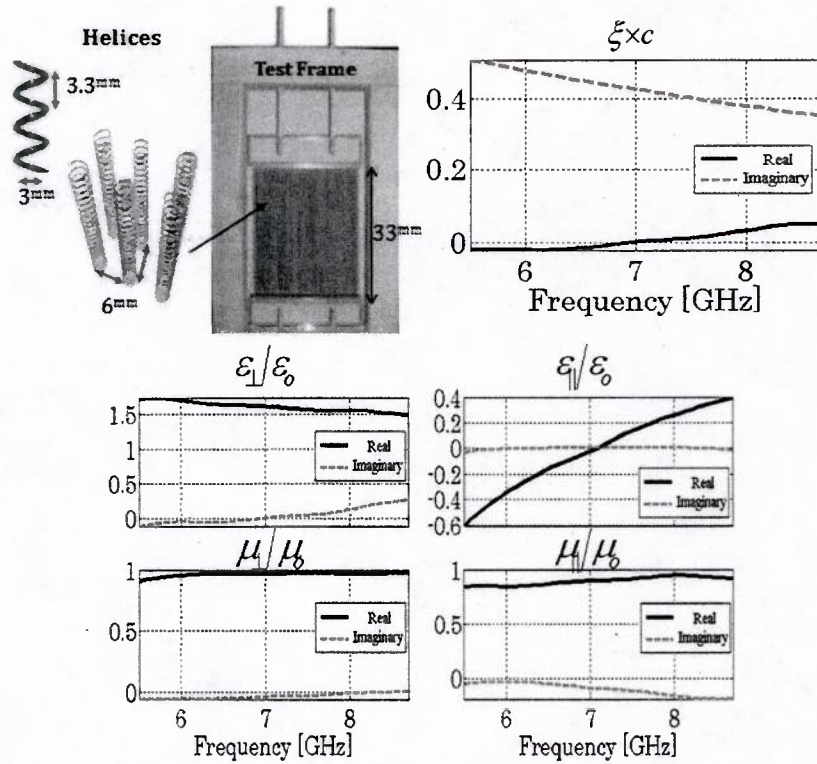


Fig. 53: Extraction of chirality and other electromagnetic constitutive parameters based on TRL measurement at multiple incidence polarizations. Top left shows the sample, its dimensions and microstructure. Top right shows the very high measured chirality. Bottom graphs show the anisotropic permittivity and permeability. Note the plasmonic response for permittivity parallel to the coils.

University of Michigan

PI: Sharon Glotzer and Nicholas Kotov

We prepared porous gold nanoparticles with unusual, angled shapes (such as nano-checkmarks) through spontaneous transformation of tellurium sacrificial templates by gradual galvanic replacement. High resolution electron microscopy studies of intermediate stages reveals interesting information regarding the replacement mechanism, involving initial “island growth” at the edges, which gradually engulfed the entire particle templates. Additionally, the high porosity of these novel nanostructures with unusual shapes is demonstrated to provide very high enhancing activity in surface enhanced Raman scattering spectroscopy. This work demonstrated that we can transfer virtually any kind of semiconductor chiral materials into plasmonic chiral structures.

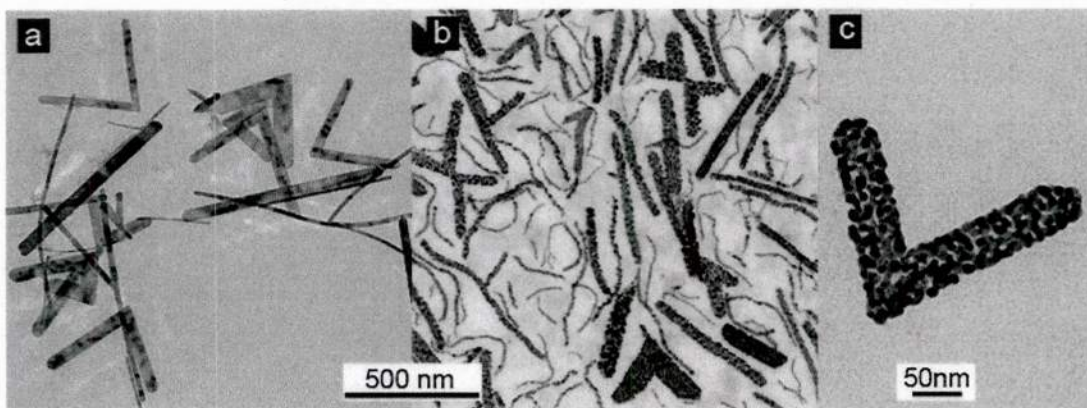


Fig. 54. TEM images of initial tellurium NPs (wires and checkmarks), before (a) and after (b) galvanic replacement with gold. (c) Higher magnification TEM image of a single gold nanoscale checkmark manifesting a rough surface and porous structure.

After that we posed the question what is the origin of chirality in the semiconductor NPs made with chiral stabilizers. It is observed in this study that the chirality of cysteine stabilizers has the distinct effect on both the growth kinetics and the optical properties of CdTe nanocrystals synthesized in aqueous solution. The effect was studied by **circular dichroism** spectroscopy, temporal UV-Vis spectroscopy, photoluminescence spectroscopy, and several other microscopy and spectroscopic techniques including atomic modeling. Detailed analysis of the entirety of experimental and theoretical data led to the hypothesis that the atomic origin of chiral sites in nanocrystals is topologically similar to that in organic compounds. Since atoms in CdTe nanocrystals are arranged as tetrahedrons, chirality can occur when all four atomic positions have chemical differences (Fig. 55). This can happen in apexes of nanocrystals which are the most susceptible to chemical modification and substitution. Quantum mechanical calculations reveal that the thermodynamically preferred configuration of CdTe nanocrystals is S type when the stabilizer is D-cysteine and R type when the L-cysteine is used as the stabilizer, which correlates

well with the experimental kinetics of particle growth. These findings help understanding the nature of chirality in inorganic nanomaterials, methods of selective production of optical isomers of nanocrystals, influence of chiral biomolecules on the nanoscale crystallization, and practical perspectives of chiral nanomaterials for optics and medicine.

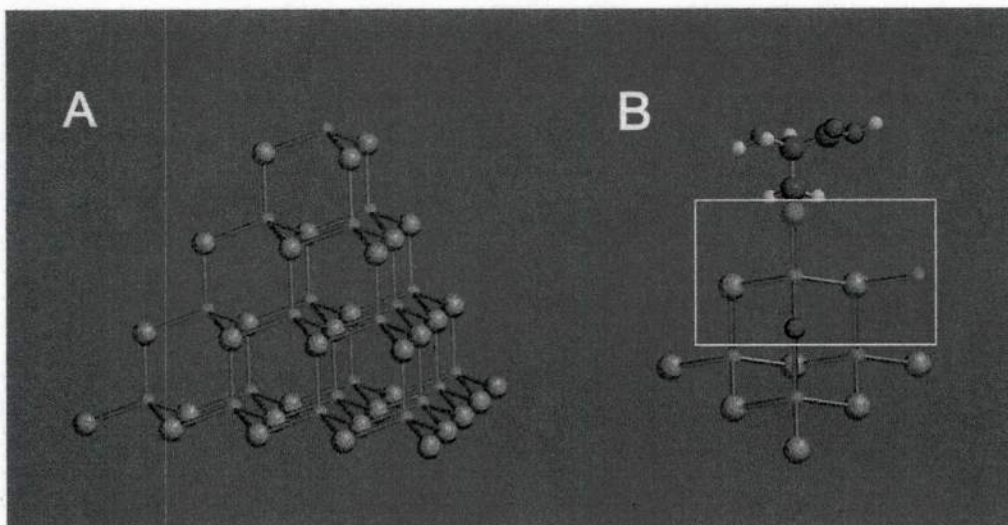


Fig. 55. (A) The ideal tetrahedron of CdTe NCs used in calculations and (B) the model of the chiral tetrahedral apex ; Cd (green); Te (brown); O (red); S (cyan).

In a parallel effort in collaboration with Prof. Yurii K. Gun'ko, we also showed that the utilisation of chiral penicillamine stabilisers allowed the preparation of new water soluble white emitting CdS nano-tetrapods (Fig. 56), which demonstrated circular dichroism in the band-edge region of the spectrum.

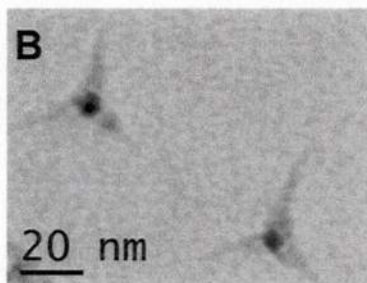


Fig. 56. High Res TEM image of chiral tetrapods.

The breakthrough in the work happened when in a joint effort between Kotov and Glotzer. We showed that the collective properties of nanoparticles manifest in their ability to self-organize into complex microscale structures. Slow oxidation of Te^{2-} in CdTe nanoparticles results in the assembly of 1 to 4-micrometer long flat ribbons made of several layers of individual CdS/CdTe nanocrystals (Fig. 57). Twisting of the ribbons with an equal distribution of left and right-helices was induced by illumination with visible light. The pitch lengths (250 to 1500 nanometers) varied with illumination dose, ribbons caused by photooxidation of CdS.

Unusual shapes of multiparticle assemblies, such as ellipsoidal clouds, dog-bone agglomerates, and ribbon bunches, were observed as intermediate stages. Computer simulations revealed that the balance between attraction and electrostatic repulsion determines the resulting geometry and dimensionality of nanoparticles assemblies. and the twisting was associated with the relief of mechanical shear stress in the assembled ribbons.

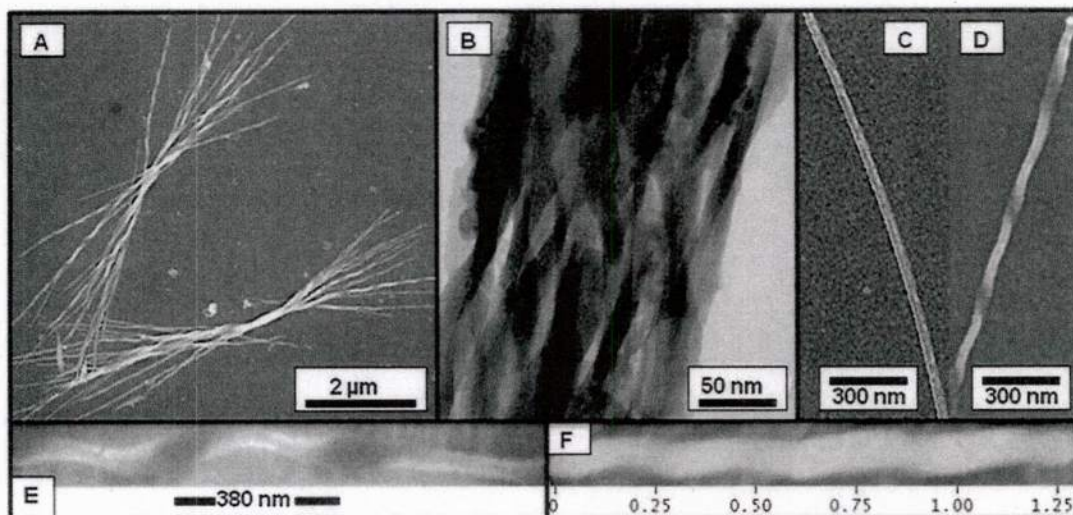


Fig. 57. (A) Scanning electron microscopy (SEM) and (B) Transmission electron microscopy (TEM) image of bundles of TRs. Individual straight NWs (C) and TRs (D). SEM (E) and Atomic Force Microscopy (AFM) images (F) of individual TRs for determination of pitch length: 380 nm (SEM) and ~ 400 nm (AFM).

We hypothesized that chiral metallic nanohelices have many unique optical and electronic characteristics that make them applicable in metamaterials and other areas of materials science. Current synthetic techniques such as DNA templating and lithography are limited in the geometries, resulting structures, and pitch lengths. The periodicity of helices in the submicron region is particularly difficult to obtain, while being critical for NIMs. In a follow-up study, we are able to synthesize helical structures from metallic gold with 220 nm pitch length by reacting gold (III) chloride with CdTe twisted nanoribbons. The synthesis for complemented by the computer modeling of their optical performance. Oxidation of CdTe nanoribbons by Au (III) initially leads to the intermediate stage of CdTe nanoribbons spotted with gold nanoparticles, and eventually results in complete replacement of CdTe with gold replicating the shape of the original twisted nanoribbons whose pitch can be varied from 200nm to 1500 nm. Such gold helices were found to decrease the transmission parameter for light in a broad range of wavelengths centered around the Au helix pitch length. Also important, these helices are highly effective at the rotation of polarized light at the wavelength corresponding to their pitch length. Interestingly, the chiro-optical performance of helical NP assemblies is predicted to be better than that of solid gold nanowires with similar geometries, which sets an important target for the

design of metamaterials. The produced gold helices with chiral purity may offer new conceptually new choices for the design of NIMs and other optical devices.

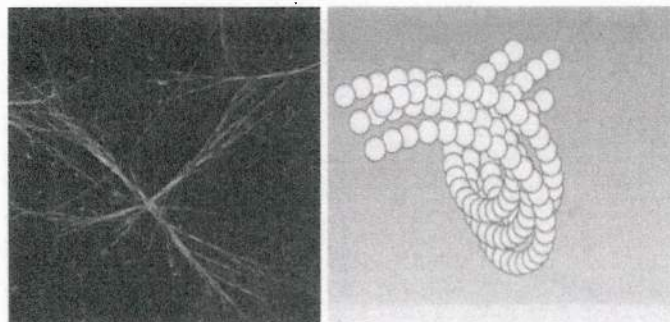


Fig. 58. (A) TEM image of Au NP helices and (B) their computational model.

Finally, in another breakthrough finding we discovered that chiral plasmonic systems can be synthesized in a very simple way using Au NP assemblies connected by DNA. Polymerase chain reaction (PCR) was realized on the surface of gold nanoparticles (NPs) as a tool for self-organization at nanoscale and as a step toward programmable production of sufficient quantities of functional metallic superstructures (Fig. 59). The assembly is controlled by varying the density of the primer on the surface of gold NPs and the number of PCR cycles generating a mixture of dimers, trimers, tetramers, etc., with gradually increasing complexity. This process leads to strong chirality of the assemblies arising from the three-dimensional positioning of NPs in space which had never been observed before. A circular dichroism band of the superstructures coincides with the plasmon oscillations of the multi-NP systems of Au colloids. This new collective optical property of NPs embracing the diversity of shapes and diameters in the starting dispersions opens unique opportunities for the development of negative index materials.

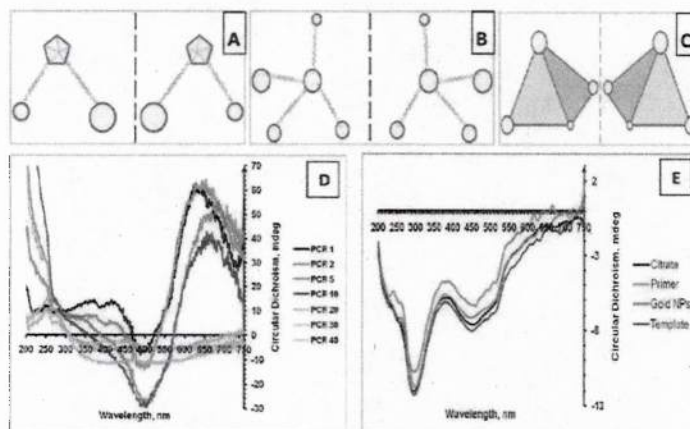


Fig.59. (A-C) Schematics of chiral NP superstructures. (D, E) Circular dichroism spectra of (D) products of PCR for increasing number of cycles, and (E) solutions of assembly components.

Notice the difference in scales for vertical axes in (D) and (E).

We simulated the self assembly of polyhedrally shaped nanoparticles, starting with tetrahedra, to investigate their potential role in soft optical NIMs and other metamaterials.

In collaboration with Palffy, Glotzer predicted, using Monte Carlo computer simulations, that hard, perfect tetrahedra can self-assemble into a complex quasicrystalline phase, opening up the possibility of fabricating the first quasicrystal made out of a single nanoparticle building block with previously unexplored physical properties. This work was published in Nature and received an extraordinary amount of press and attention [30]. A follow-up paper exploring the stability of the quasicrystal phase relative to another higher density phase was reported by us, demonstrating that the QC should be stable at packing fractions up to 83%, and thus observable in experiments [31].

Due to advancements in the synthesis of non-spherical nanoparticles, the phase behavior of polyhedral shapes is becoming of increasing interest. Regular tetrahedra have attracted particular attention, because they prefer local symmetries, which are not compatible with periodicity. Two dense phases of regular tetrahedra were reported during the lifetime of this grant:

1. The densest known tetrahedron packing is achieved in a crystal of triangular dipyrramids (dimers) with packing fraction $4000/4671 \approx 85.63\%$.
2. In simulation a dodecagonal quasicrystal is observed; its (3,4,32,4) approximant can be compressed to a packing fraction of 85.03%.

We showed that the approximant is more stable than the dimer crystal for packing densities below 84% using Monte Carlo simulation and free energy calculations. The enhanced stability of the approximant can be attributed to a network substructure which allows particles to have bigger moving spaces as evident from free volume calculations; it also facilitates correlated motion of particles, which further contributes to entropy. The existence of a solid-solid transition between structurally distinct phases not related by symmetry breaking, e.g. the approximant and the dimer crystal, is unusual in hard particle systems. Hard tetrahedra are the first example of hard particles with two distinct solid phases not mutually related by symmetry breaking. This shows that entropic effects alone are sufficient for inducing such nontrivial solid-solid phase transitions.

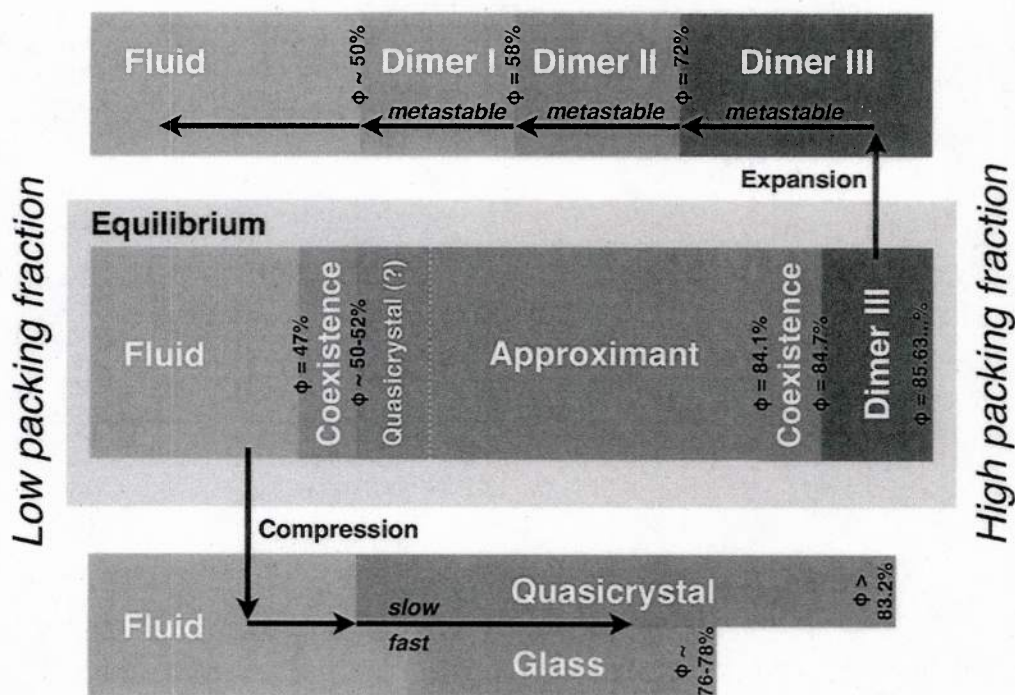


Fig. 60. Schematic phase diagram of hard tetrahedra summarizing our findings. In thermodynamic equilibrium the dimer III crystal and the approximant are stable. In compression simulations the approximant is never observed. Instead, a quasicrystal is grown. If crystallization is suppressed, then a glass with local tetrahedral order forms. The transformation of the approximant or quasicrystal to and from the dimer III crystal cannot be observed in simulation. Instead the dimer III crystal transforms into the dimer II crystal, and then the dimer I crystal during expansion before it melts.

The assembly of hard particle shapes into novel ordered structures has received much attention in recent years. Under this effort, we focused on triangular bipyramids, which pack densely in a simple triclinic crystal with two particles per unit cell. We show that triangular bipyramids do not form this packing in simulation. Instead, they assemble into a dodecagonal quasicrystal, which is similar to the quasicrystal recently discovered in the hard tetrahedron system.

This new formation is only the second quasicrystal formed with hard particles and the first one that is degenerate. Thermodynamic integration revealed that the triangular bipyramid quasicrystal or an approximant thereof is thermodynamically favored over the triclinic crystal up to very high packing fractions. These results highlight the fact that entropy may play a much larger role in quasicrystal formation than has been previously thought.

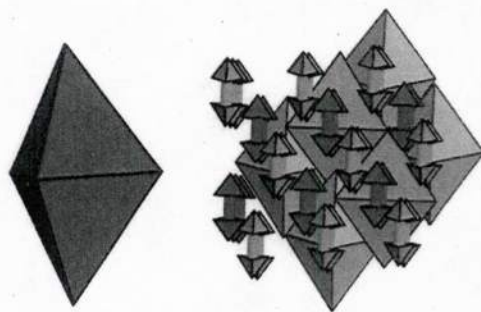


Fig. 61. Illustration of triangular bipyramid, TBP.

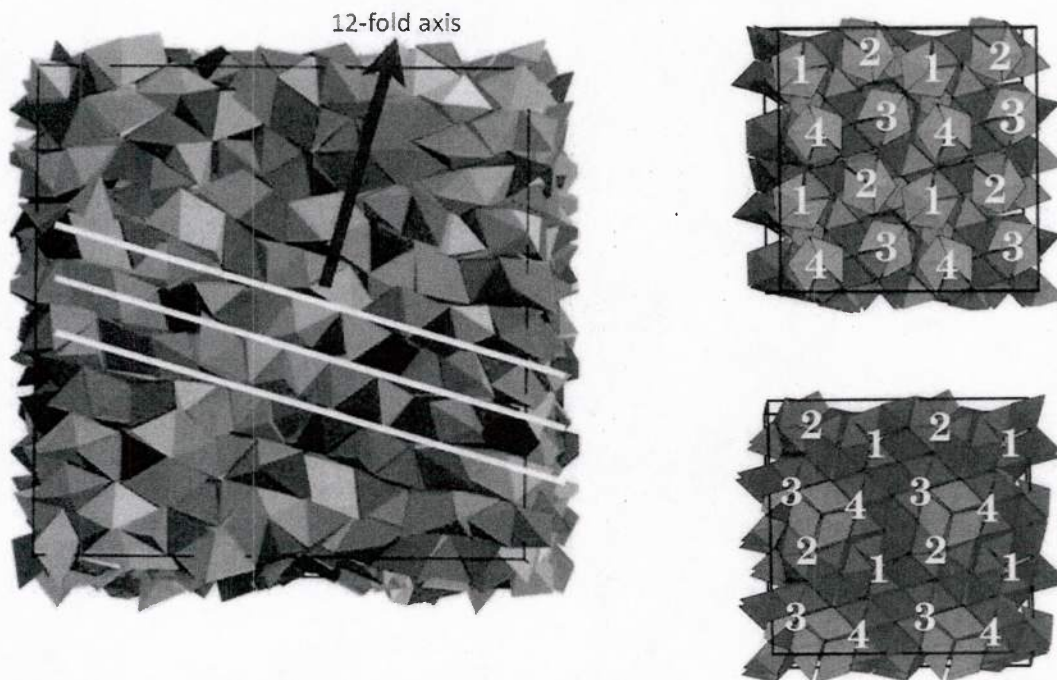


Fig. 62. Degenerate quasicrystal and quasicrystal approximants.

Remarkably, hard TBPs not only prefer a complex quasicrystal over the simple TBP crystal, but also form it in timescales comparable to that previously observed in the hard tetrahedron system. This is surprising since, in comparison to tetrahedra, the highly anisotropic TBPs are far more constrained. Thermodynamic stability of the DQC and DA can be attributed to the additional configurational entropy associated with collective motion of particles as well the clustering entropy; none present in the TBP crystal. Quasicrystal's degeneracy helps it form so easily in simulation as random pairing allows TBPs to join existing seeds of the QC without forming configurations that are kinetically trapped due to inappropriate pairing. Particle rearrangements needed for the formation and growth of the seed are also feasible due to local similarity of the fluid and the DQC.

Obtaining a quasicrystal from tetrahedrally shaped nanoparticles can be hampered by many practical limitations such as shape variations, polydispersity and softness of the interaction potential – factors that have not been taken into account in previous works. From a theoretical point of view, a full description of the formation and underlying thermodynamics is challenging and many questions remain open. Using Monte Carlo and Molecular Dynamics computer simulations, we investigated the effect of particle imperfections on the assembly propensity of nanotetrahedra. We have studied the role of geometric and chemical imperfections of nanotetrahedra on the formation of the quasicrystalline phase predicted to occur in the system of hard, perfect tetrahedra. As summarized in table F1, the formation of the quasicrystal is extremely robust. We confirm its stability for a considerable range of perturbations in shape and particle interactions. The values found in this work, if taken individually, are compatible with most experimental techniques fabricating anisotropic shapes. Although a combination of imperfections (e.g. truncation and softness) will be present in experiments, our results confirm that the formation of the quasicrystal should be feasible experimentally, if the nanotetrahedra are equilibrated at the correct packing density. We expect this work to serve as a guide not only for experimentalists trying to assembly the tetrahedra quasicrystal, but also as an example on how particle imperfections of nanoscopic building blocks can be expected to affect the crystallization process. [Damasceno, et al, in preparation]

Type of imperfection	Range of QC stability	Uncertainty	Experimental realization
Roughness	$L \geq 5$	$L = 4$	Homoz & Brenner, 2011; Manoharan et al., 2003
Roundedness	$R \leq 40\%$	$R = \pm 5\%$	Berenschot, Tas, Jansen, & Elwenspoek, 2009a; Greyson, Barton, & Odom, 2006; Jaoshvili et al., 2010
Truncation	$T \leq 25\%$	$T = \pm 5\%$	Berenschot, Tas, Jansen, & Elwenspoek, 2009a; Chiu et al., 2011; Greyson, Barton, & Odom, 2006
Polydispersity	$p \leq 10\%$	$10\% \leq p \leq 15\%$	Berenschot et al., 2009; Manoharan et al., 2003
Softness	$s \geq 5$	$s = 4$	Manoharan et al., 2003

Table F1: Summary of the parameter ranges necessary for the self-assembly of the quasicrystal for each of the five types of imperfections. The given range of stability corresponds to the successful formation of the quasicrystal in simulation.

An interesting outcome from our studies was the discovery that faceting of nanoparticles (in special, tetrahedra) could lead to the generation of a variety of complex structures. Among those, special excitement regards the possibility of assembling a diamond lattice in the nanoscale, opening a path for a bottom-up approach able to assemble wide and complete

photonic band gap materials. The observation that the structures were primarily composed of face-sharing polyhedra led us to rationalize the assemblies in terms of a new concept of directional entropic forces (DEF), that could not only explain the formation of such structures but potentially give directions towards predictability and rules for reverse engineering of particular structures with interesting (e.g. photonic) properties. In order to test these ideas, we decided to perform a systematic study of hundreds of polyhedra that could allow us to relate the shape of different building blocks to the structures that would spontaneously form from them [32].

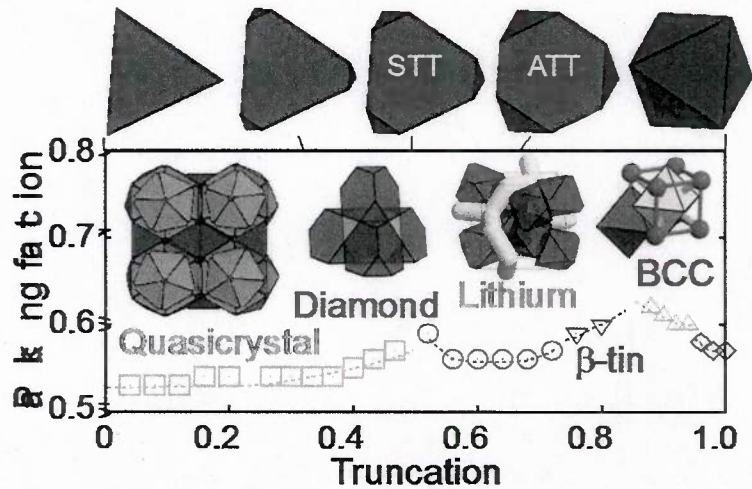


Fig. 63. Phase diagram of truncated tetrahedra. Data sets correspond to the lowest density, ϕ_c , at which crystallization from the fluid is observed. Labels indicate the dodecagonal quasicrystal, diamond, β -tin, high-pressure Li, and body-centered cubic structures that were found to self-assemble.

In this context, our recent *Science* publication, "Assembly of Polyhedra into Complex Structures,"[33] represents an exciting advance in the problem of self-assembly, showing that a surprising degree of complexity is possible from shape alone. Our findings isolate and demonstrate the important role of entropy in this ubiquitous phenomenon, and we reported the findings of detailed Monte Carlo simulations of the thermodynamic self-assembly of 145 hard convex polyhedra. Shapes investigated include all the Platonic, Archimedean, Catalan and Johnson solids, and some zonohedra, prisms and antiprisms, constituting the most comprehensive single study of thermodynamic self-assembly of hard colloids ever reported.

We showed that 101 of the 145 shapes assemble into an ordered phase, demonstrating an unexpectedly high propensity for order in hard polyhedra. Among these 101 assemblies, we report 22 Bravais and non-Bravais crystals, two quasicrystals, 66 plastic crystals (both Bravais and topologically close-packed), 21 liquid crystals (nematic, smectic, and columnar), and 44 glasses, demonstrating a diversity of structure that is unprecedented for hard particles. We present some of the most complex crystalline phases yet observed in a non-atomic system, including a colloidal crystal identical to that of gamma brass with 52 particles in the unit cell.

The plastic rotator phases are unusual and have no analog in atomic systems, and the glasses we present - 44 different particles that never order on the long time scales of our simulations - are remarkable in that 41 of them are Johnson solids and most are non-centrally symmetric.

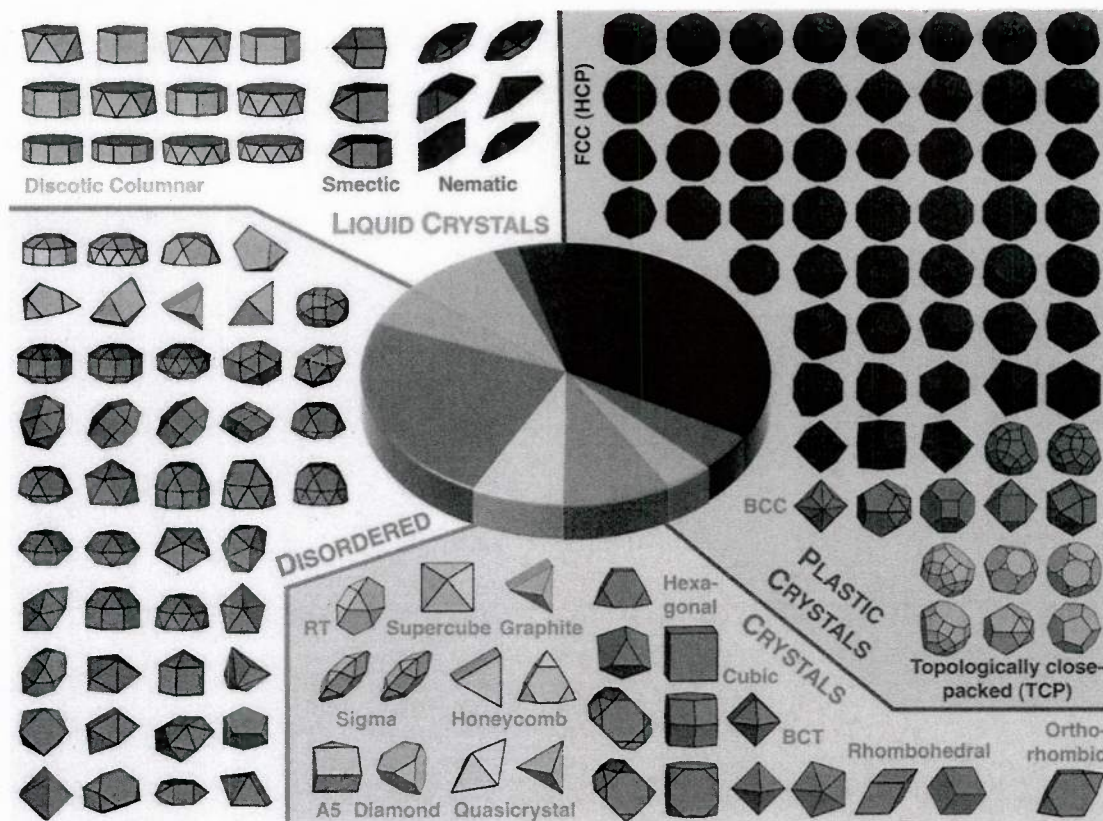


Fig. 64. Polyhedra are separated into four categories of organization as indicated by different colors: liquid crystals, plastic crystals, crystals, and disordered (glassy) phases. Subcategories (classes) are indicated by shades. The assembly category of liquid crystals contains the classes discotic columnar, smectic, and nematic (different shades of pink). Plastic crystal classes are FCC (dark blue), BCC (blue), and TCP (light blue). In the case of crystals, we distinguish Bravais lattices (dark green) and non-Bravais lattices (light green). RT stands for random tiling. For the glasses, no assembly is observed, and we distinguish those that strongly order locally with preferential face-to-face alignment (light orange) from those with only weak local order (dark orange). The pie chart in the center compares the relative frequency of the 10 observed classes. In each of the classes, polyhedra are listed in decreasing order of the isoperimetric quotient. A polyhedron is included multiple times if it was found to assemble into more than one ordered structure [33].

Because of the vast amount of data collected for this study, we were able to take an important step forward in structure prediction and relate particle shape to assembled structure in a way not previously possible. Specifically, we demonstrated that the isoperimetric quotient – a simple measure of particle shape – and the number of neighbors in the first neighbor shell of the dense fluid -- a quantity easily measured in experiment or simulation prior to assembly -- can be

combined to predict the structural class of the ordered phase. These findings will provide guidance to experimentalists in the design and fabrication of nano particle and colloidal systems, including those with weak interactions in which entropy plays an important role, and are relevant to such disparate problems as virus and protein crystallization.

Wake Forest University

PI: David Carroll

Abstract

The WFU component of the MURI focused on the use of aligned Ag nanowires in alumina templates to create a slab (flat) metalens. These lenses are expected to be hyperbolically dispersive. The characteristics we studied in detail are: the lenses' ability to focus (image) and negative refraction. Part I of our studies involved the creation of large area slab lenses. These should have optical quality surfaces with little spurious scattering due to surface defects. Part II then characterized the slabs using reflectometry and transmission so that the wavelength regions of "negative refraction" behavior could be determined. Finally, in Part III, we imaged with the slabs and determined image formation distances using NSOM together with detailed modeling of diffraction by the object. The results are that we were able to create a slab lens with imaging capabilities and enhanced transmission relative to thin films and other nanorod arrays reported.

Impacts

This work has potential applications in compact IR antennae design and microphotronics switching as well as advanced imaging for diagnostics. Several of the lenses are under study for use in nano-raman systems currently.

Part I: lens fabrication

It was determined early on that the published routes to nanorod arrays were inadequate for the formation of optical quality lenses. In the literature, FIB formed lenses have shown the best quality (Stanford). This approach however shows little hope of scaling to the sizes necessary for real applications. Published electrochemical routes typically leave barrier layer remnants that lead to excessive scattering for very thin slabs. To achieve actual imaging this would have to be overcome.

Our approach was to use a number of finishing steps after the electrochemical etching and addition of metals. To begin, Al is anodized under constant voltage at 1°C for > 6 hrs. Voltage and acid bath determine pore size and spacing. Then AAO is removed with chromic and phosphoric acid at 70°C for 6 hrs. A 2nd anodization results in hexagonal array of pores. Anodization time sets membrane thickness. Pores widened in acid such as phosphoric acid. The barrier layer is thinned by gradually reducing the potential to 10V. We then achieve "tuning" control over the template properties. Fig. 65 (A) shows an AAO template grown in oxalic acid, then pore-widening in H₃PO₄ (B) 30 minutes, (C) 37 minutes, and (D) 42 minutes. The template growth procedure coupled with pore-widening allows us to precisely manufacture these materials and to tune the optical constants.

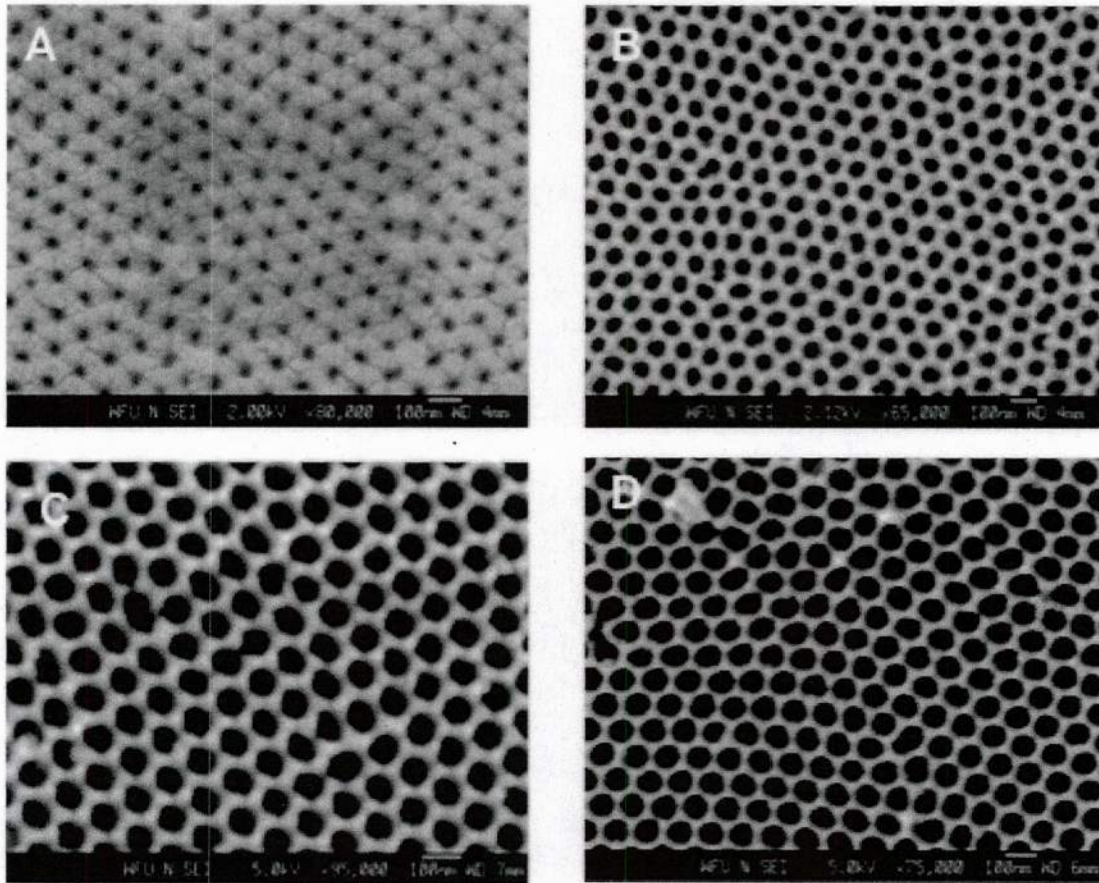


Fig. 65: Template formation using our new polishing procedure

Once the templates are formed the metals are added. We used Ag for the nanorods. The new etching procedures allow for spacing-diameter relationships which better match those studied by the Iowa State group as shown in Fig. 66.

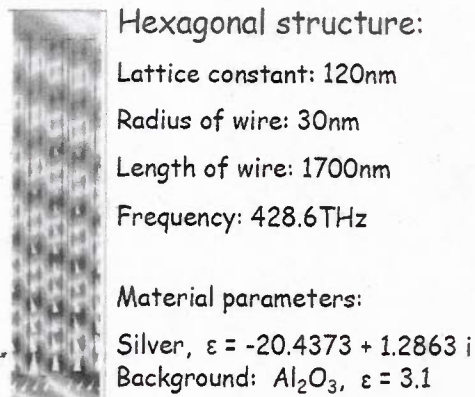


Fig. 66: calculations done by the IA State group for our systems.

With the addition of the Ag into the template (shown in fig. 67) we were then able to add a PMMA coating to provide a low index support feature. As seen in fig. 67 this results in a

translucent slab (it is held at an angle in the photo) with excellent transmission off the plasmon resonance.



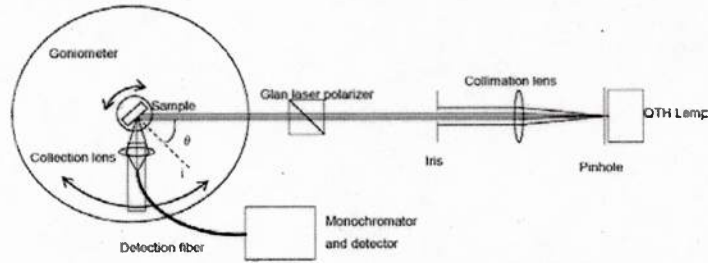


Fig.68: experimental setup

We examined the reflectometry of a variety of nanowire arrays in AAO. These arrays were made with varying wire spacing, metal density, and thickness. For each sample Brewster's angle was determined as a function of wavelength both above and below the plasmon resonance as determined by transmission spectroscopy. The best data is shown in fig. 69 below.

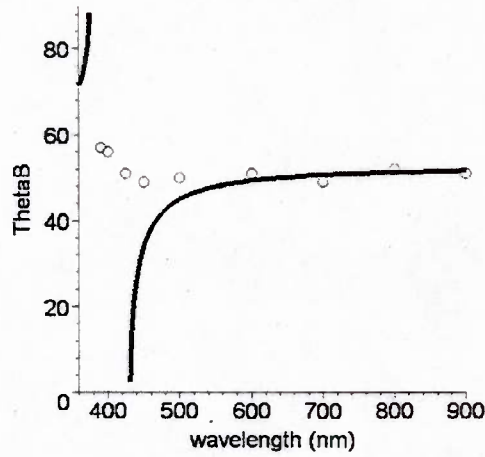


Fig. 69: experimental data of the observed Brewster's angle (circles) plotted together with the calculated values for the array based on Maxwell-Garnett theory.

The data shown in fig. 69 is for an eight micron thick slab with a metal filling ratio (p) of 0.35. Rods are approximately 6-7 microns long, and 20 nm in diameter. The bandwidth of the spectrometer is approximately 10 nm. The solid curves represent the calculated values using:

$$\theta_B = \begin{cases} \arctan \left(\frac{\sqrt{\epsilon_{//}(\epsilon_{//} - 1)(\epsilon_{\perp} - 1)} \sqrt{(\epsilon_{//} \epsilon_{\perp} - 1)(\epsilon_{//} - 1)}}{(\epsilon_{//} - 1)(\epsilon_{//} \epsilon_{\perp} - 1)} + i \frac{\sqrt{(\epsilon_{//} \epsilon_{\perp} - 1)(\epsilon_{//} - 1)}}{\epsilon_{//} \epsilon_{\perp} - 1} \right), & \epsilon_{//} \text{ and } \epsilon_{\perp} > 0 \\ \arctan \left(\frac{\sqrt{\epsilon_{//}(\epsilon_{//} - 1)(\epsilon_{\perp} - 1)} \sqrt{(\epsilon_{//} \epsilon_{\perp} - 1)(\epsilon_{//} - 1)}}{(\epsilon_{//} - 1)(\epsilon_{//} \epsilon_{\perp} - 1)} - i \frac{\sqrt{(\epsilon_{//} \epsilon_{\perp} - 1)(\epsilon_{//} - 1)}}{\epsilon_{//} \epsilon_{\perp} - 1} \right), & \epsilon_{//} * \epsilon_{\perp} < 0 \end{cases}$$

for wavelengths above and below the plasmon resonance of approximately 420nm. As far as we have been able to determine this is the shortest wavelength for the onset of hyperbolic dispersion and negative epsilon measured. Furthermore, unlike the measurements cited in literature, this shows the effect occurring at the plasmon resonance as predicted by theory. I note here that a

similar measurement published late last year demonstrate a similar effect for longer wavelengths, but negative refraction occurs in that work, clearly in the area of elliptical dispersion!

Summary: From this we can say that we have been successful in creating a negative refraction material using the new procedure for the production of “transparent” large area slabs. The transmission of light is greater than that of published meta-slabs. Now the question remains, can one image with this?

Part III: Imaging

To examine the imaging quality of the slab, we must use an object wherein the resolution of the image can be determined. Previous work in this area projected the image onto a substrate coated with photoresist and then imaged the photolithographed object. We desired a more direct conformation of imaging. A number of experimental setups were attempted, but difficulties with identifying the nano-object to be imaged prevented unambiguous determination of the image distance. We finally hit upon the idea of using a NSOM to record images along with image plane distances from an object illuminated with polarized and coherent radiation near the plasmon resonance. Thus the setup is analogous to illuminating an object with parallel light beams and determining the image distance formed through a lens. At distances close to the slab, this appears as a Fresnel diffraction pattern. We chose two different objects to image: a parallel set of lithographed metal lines, and a nanoparticle of metal. These two objects should present a completely isotropic diffraction pattern in the image plane.

Imaging Experiments with slab lenses

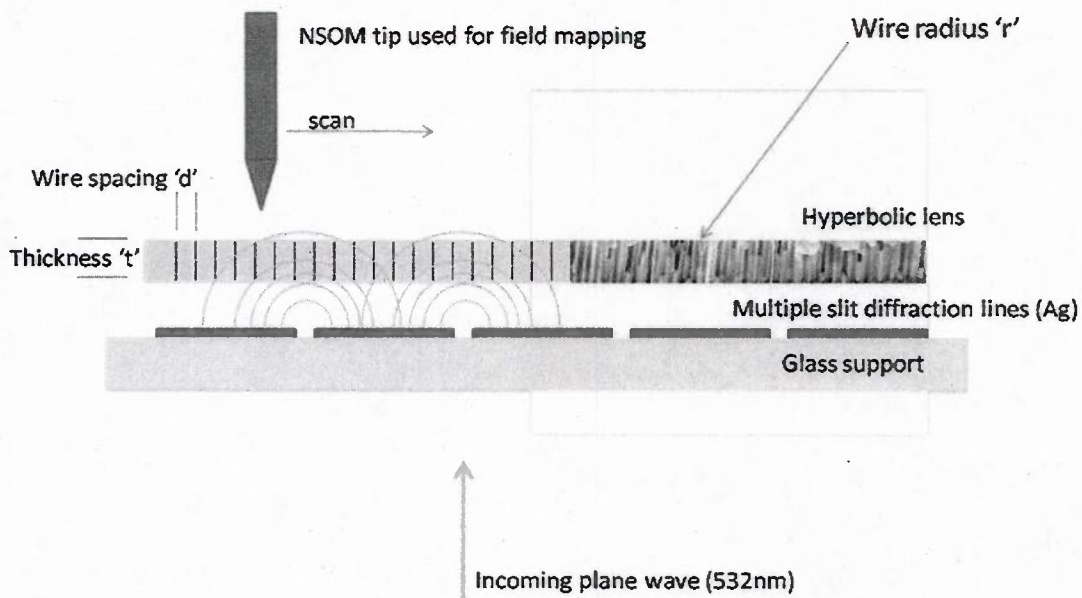


Fig. 70a: The experimental setup for imaging diffraction patterns through a slab lens (as shown before). This is shown for parallel lithographed lines.

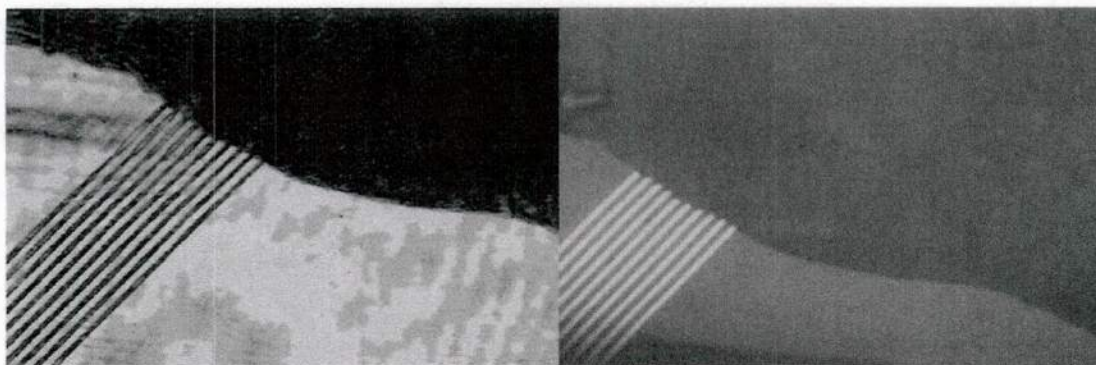


Fig. 70b: this shows the slab sitting on top of the parallel lithographed lines. The NSOM tip as scanned above this slab and above the lines. We can compare the image formed in air (positive index) and above the slab (negative index).

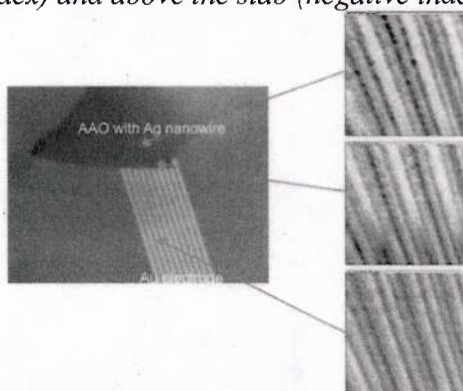


Fig. 70c: images collected in constant height mode of NSOM show the Fresnel diffraction of the object and how these patterns change across the lens edge. By comparing the diffraction patterns we can determine the change in path length through the lens as long as we know exact heights.

As described above, in this experiment we attempted to determine the actual optical path length change through the lens near resonance. The idea is to image the field intensity with a scanning near field microscope tip, above the sample (which is the wires in this case). The height of the tip is held constant and the Fresnel diffraction fringes were imaged. Thus we have an image of the diffraction pattern in the plane ~ 120 microns above the sample. A typical image is shown in fig. 71.

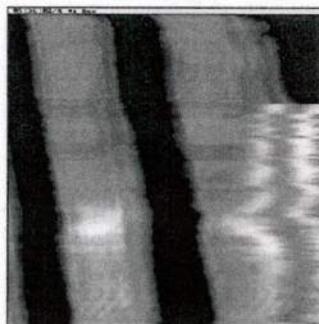


Fig. 71: a typical diffraction image above the diffraction grating without a meta-lens in place. This image was collected very close to the grating and the smearing on the right is where the tip made contact with the surface.

These images were then collected (at the same height exactly) above the sample and through the lens. Literally hundreds of heights and diffraction patterns were calculated and matched to the observed data.

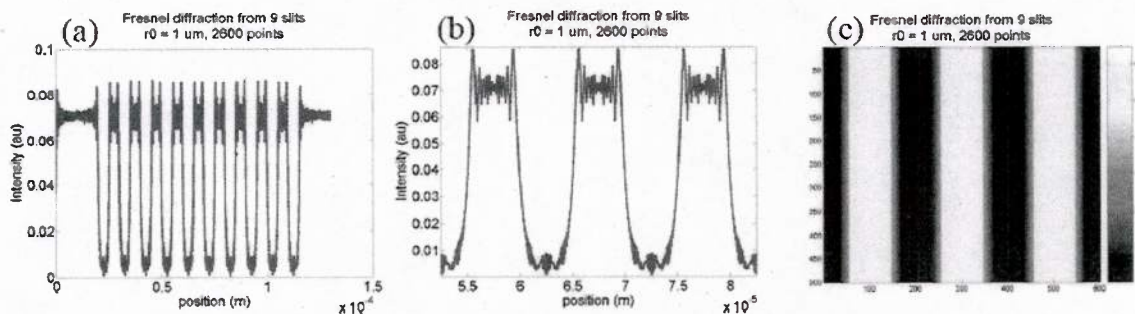


Fig. 72: A typical calculated Fresnel diffraction pattern above the sample for a given height.

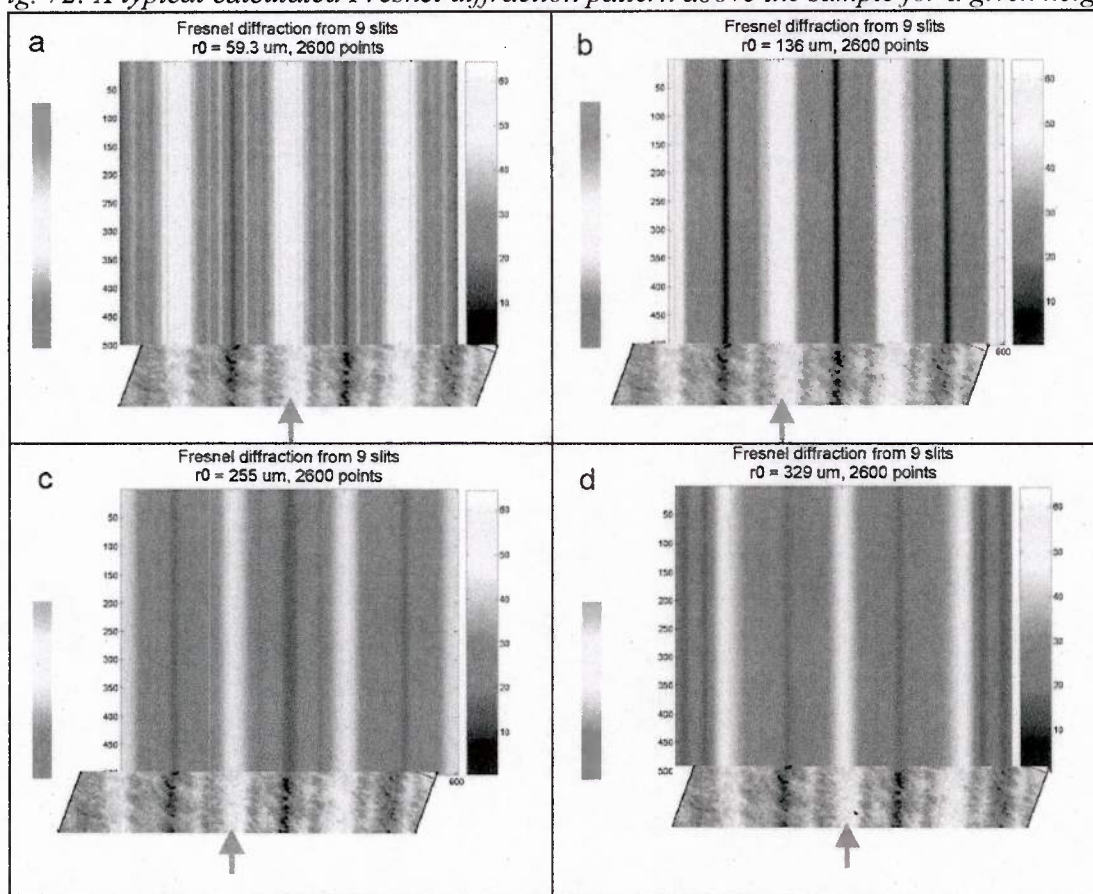


Fig. 73: comparisons of diffraction patterns and calculations were made by aligning fringes. The free variable in the calculation was the tip height (which could then be determined independently).

Comparisons were made between the calculated patterns and the observed patterns to determine the “apparent height” above the sample as one observes the image through the lens, as shown in fig. 73.

In the best results of the study, we compared diffraction images occurring at ~ 151.6 microns above the diffraction grating. Without the lens, the imaged and calculated patterns for this height aligned very well, indicating that the height was well determined and the images were exactly as calculations say they should be. Then the tip was held at exactly the same height and the image observed through the lens. However in this case the observed diffraction fringes were those that corresponded to a height of 59.3 microns. Several experiments were done to confirm this finding. Furthermore, without the metal filling (using only the AAO), the measured height was nearly unaltered.

The second set of objects we studied was nanoparticles of Ag supported on the mica substrates and illuminated from behind again using the parallel beam light. The experimental setup remained the same, and the experimental technique was the same. Ag nanoparticles of approximately 20 nm were placed on the mica substrate in solution and allowed to dry. The lens was then placed on top of this sample and the image was collected by NSOM in constant height mode. This was done for a wide variety of lens thickness's. Shown here are the best results.

The nanoparticles yield a circular diffraction pattern. Typical images are shown here in fig. 74.

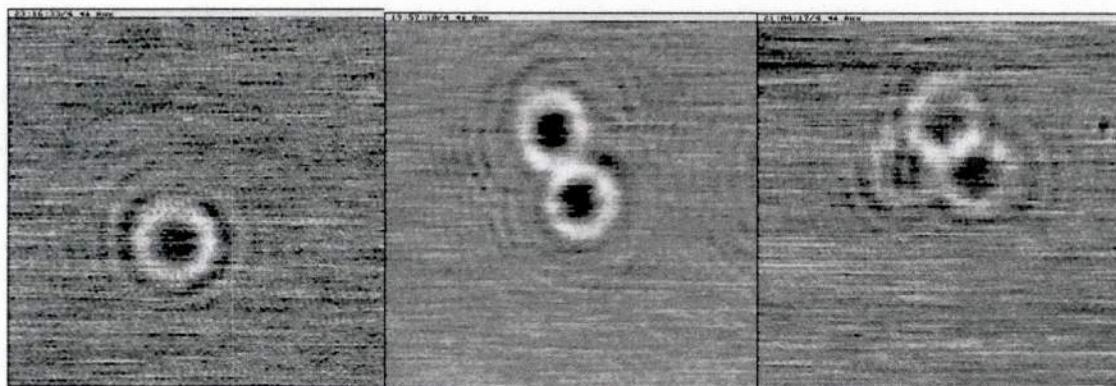


Fig. 74a: left to right shows images collected in constant height mode NSOM of 1, 2, and 3 metal nanoparticles. The nanometals are illuminated from underneath as shown above.

Fig. 74b: the experimental setup and images collected at different heights above the substrate with no slab.

Adding the slab reduced light considerably. As shown in fig. 75, a similar sequence of images can be achieved over the nanoparticles with the slab in place.



Fig. 75 shows a nanoparticle imaged on the substrate at a given height (11 microns). The image on the right is a particle imaged through the lens at the same height. Notice that the ring size is now smaller, indicating that in this imaging plane the particle has appeared to move closer to the tip! To see how much closer, we must model the image and this is still underway.

Summary: from these first attempts to image with the slab lens we can say that there is an apparent image formation through the lens. This image is consistent with imaging through a negative index material.

Finally:

We have continued to push the envelope on slab formation. By altering the voltage prescription during pore formation, we have been able to achieve forked nanorod substrates with a similar surface quality of our straight nanorods. Shown in fig 76. Conceptually such substrates could exhibit true negative index behavior because they can have a magnetic component associated with inductance in the fork itself. We do not yet have optical data on these.

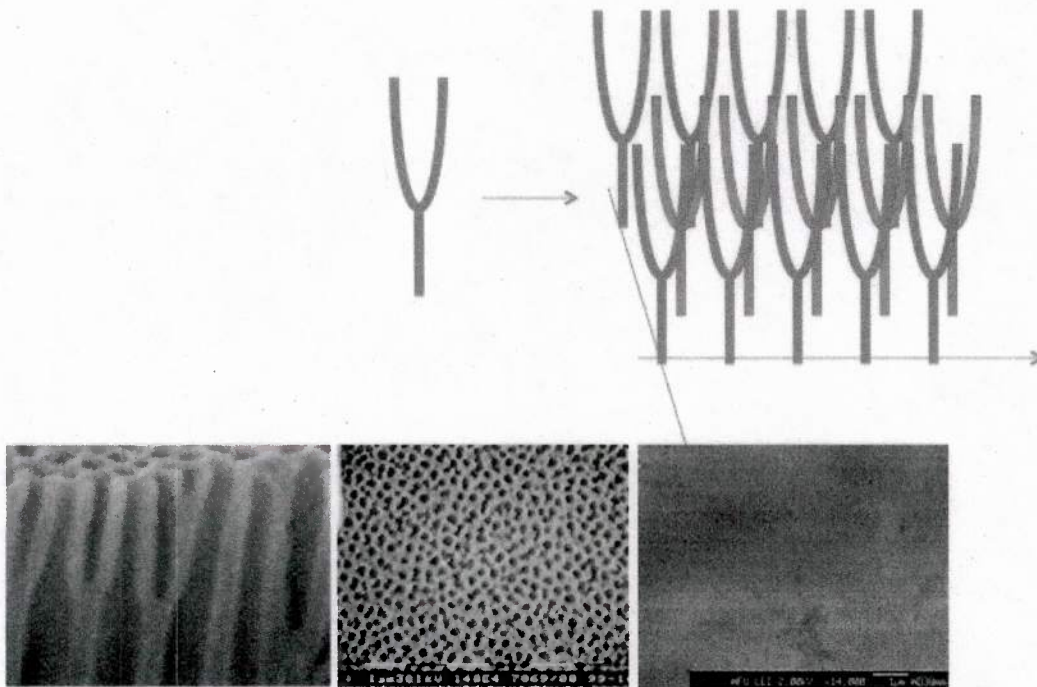


Fig. 76: new forked substrates ready for testing.

Our group is continuing to examine these substrates for true negative index characteristics.

Summary

Our goal was to create a negative index slab lens that could be used in imaging. The results are a new electrochemical method for making hyperbolically dispersive lenses that are of

optical quality over larger areas and with different nanowire spacing than previously reported. Using reflectometry we have determined that a negative index behavior can be seen where it is expected, unlike previous reports and confirming current calculational models. When used in imaging, these lenses form images that are consistent with a negative index material. As a final step in the program, improvements to the lens structure have been created using forked nanowires. These are now undergoing optical testing.

Personnel supported throughout this program:

Baxter McGuirt – Masters student

Jerry Keilbasa – PhD student

Junping Zhang – postdoc

References

- [1] A. Fang, Th. Koschny, and C. M. Soukoulis, "Optical anisotropic metamaterials: Negative refraction and focusing", *Phys. Rev. B* 79, 245127 (2009).
- [2] E. Plum, J. Zhou, J. Dong, V.A. Fedotov, Th. Koschny, C.M. Soukoulis, and N.I. Zheludev, "Metamaterial with negative index due to chirality", *Phys. Rev. B* 79, 035407 (2009).
- [3] J. Zhou, J. Dong, B. Wang, Th. Koschny, M. Kafesaki, and C.M. Soukoulis, "Negative refractive index due to chirality", *Phys. Rev. B* 79, 121104(R) (2009).
- [4] B. Wang, J. Zhou, Th. Koschny, M. Kafesaki, and C.M. Soukoulis, "Chiral metamaterials: Simulations and experiments", *J. Opt. A: Pure Appl. Opt.* 11, 114003 (2009).
- [5] B. Wang, J. Zhou, Th. Koschny, and C.M. Soukoulis, "Nonplanar chiral metamaterials with negative index", *Appl. Phys. Lett.* 94, 151112 (2009).
- [6] B. Wang, Th. Koschny, and C.M. Soukoulis, "Wide-angle and polarization-independent chiral metamaterial absorber", *Phys. Rev. B* 80, 033108 (2009).
- [7] J. Dong, J. Zhou, Th. Koschny, and C.M. Soukoulis, "Bi-layer cross chiral structures with strong optical activity and negative refractive index", *Opt. Express* 17, 14172 (2009).
- [8] J. Zhou, Th. Koschny, M. Kafesaki, and C.M. Soukoulis, "Negative refractive index response of weakly and strongly coupled optical metamaterials", *Phys. Rev. B* 80, 035109 (2009).
- [9] D.O. Guney, Th. Koschny, C.M. Soukoulis, "Reducing ohmic losses in metamaterials by geometric tailoring", *Phys. Rev. B* 80, 125129 (2009).
- [10] D.O. Guney, Th. Koschny, M. Kafesaki, and C.M. Soukoulis, "Connected bulk negative index photonic metamaterials", *Opt. Letters* 34, 506 (2009).
- [11] R. Zhao, Th. Koschny, E.N. Economou, and C.M. Soukoulis, "Comparison of chiral metamaterial designs for repulsive Casimir force", *Phys. Rev. B* 81, 235126 (2010).
- [12] R. Zhao, P. Tassin, Th. Koschny, and C.M. Soukoulis, "Optical forces in nanowire pairs and metamaterials", *Opt. Express* 18, 25676 (2010).
- [13] D.O. Guney, Th. Koschny, and C.M. Soukoulis, "Surface plasmon driven electric and magnetic resonators for metamaterials", *Phys. Rev. B* 83, 045107 (2011).
- [14] H. S. Park, A. Agarwal, N. A. Kotov, and O. D. Lavrentovich, 'Controllable Side-by-Side and End-to-End Assembly of Au Nanorods by Lyotropic Chromonic Materials', *Langmuir*, 24 (2008), 13833-37.
- [15] A. B. Golovin, and O. D. Lavrentovich, 'Electrically Reconfigurable Optical Metamaterial Based on Colloidal Dispersion of Metal Nanorods in Dielectric Fluid', *Applied Physics Letters*, 95 (2009)
- [16] A. B. Golovin, J. Xiang, Y. A. Nastishin, and O. D. Lavrentovich, 'Electrically Reconfigurable Optical Metamaterials Based on Orientationally Ordered Dispersions of Metal Nano-Rods in Dielectric Fluids', *Liquid Crystals* Xiv, 7775 (2010)
- [17] A. B. Golovin, J. Xiang, H. S. Park, L. Tortora, Y. A. Nastishin, S. V. Shiyankovskii, and O. D. Lavrentovich, 'Electro-Optic Effects in Colloidal Dispersion of Metal Nano-Rods in Dielectric Fluid', *Materials*, 4 (2011), 390-416.

- [18] J. Fontana, C. Grabowski, M. Ignatenko, Lei Kang, Stephan Woods, and P. Palffy-Muhoray, 'Experimental Determination of the Polarizability of Gold Nanorods in the Visible Range', *Phys. Rev. B* (to be submitted) (2012).
- [19]. M. Ignatenko, Lei Kang, C. Grabowski, G. Richards, and P. Palffy-Muhoray, 'Numerical Characterization of Bulk Susceptibility of Gold Nanorod Suspensions at Optical Frequencies', *Phys. Rev. B* (to be submitted) (2012)
- [20]. X. Y. Zheng, J. Fontana, M. Pevnyi, M. Ignatenko, S. Wang, R. Vaia, and P. Palffy-Muhoray, 'The Effects of Nanoparticle Shape and Orientation on the Low Frequency Dielectric Properties of Nanocomposites', *Journal of Materials Science*, 47 (2012), 4914-20.
- [21]. Palffy-Muhoray et al., Committee on Nanophotonics Accessibility and Applicability, National Research Council, *Nanophotonics: Accessibility and Applicability* (The National Academies Press, 2008).
- [22] L. Greengard and J.-Y. Lee, Stable and accurate integral equation methods for scattering problems with multiple material interfaces in two dimensions, *Journal of Computational Physics* 231 (2012) 2389–2395
- [23] C. L. Epstein, Z. Gimbutas, L. Greengard, A. Kloeckner, and M. O'Neil, A consistency condition for the vector potential in multiply-connected domains, arXiv:1203.3993v1, submitted.
- [24] A. Barnett and L. Greengard, A new integral representation for quasi-periodic fields and its application to two-dimensional band structure calculations, *Journal of Computational Physics* 229 (2010) 6898–6914
- [25] A. Barnett and L. Greengard, A new integral representation for quasi-periodic scattering problems in two dimensions, *BIT Numer Math* (2011) 51: 67–90
- [26] Z. Gimbutas and L. Greengard, Fast multi-particle scattering: a hybrid solver for the Maxwell equations in microstructured materials, *Journal of Computational Physics*, to appear.
- [27] C. L. Epstein and L. Greengard, Debye Sources and the Numerical Solution of the Time Harmonic Maxwell Equations *Communications on Pure and Applied Mathematics* 63 (2010), 413–463
- [28] C. L. Epstein, L. Greengard, and M. O'Neil, Debye Sources and the Numerical Solution of the Time Harmonic Maxwell Equations, II *Communications on Pure and Applied Mathematics*, to appear.
- [29] D. R. Smith, W. Padilla, D. C. Vier, S. C. Nemat-Nasser, and S. Schultz, *Phys. Rev. Lett.* 84, 4184 (2000).
- [30] Amir Haji-Akbari, Michael Engel, Aaron S. Keys, Xiaoyu Zheng, Rolfe G. Petschek, Peter Palffy-Muhoray & Sharon C. Glotzer, "Disordered, quasicrystalline, and crystalline phases of densely packed tetrahedra," *Nature* 462, 773-777 (2009).
- [31] A. Haji-Akbari, M. Engel, S. C. Glotzer, "Phase Diagram of Hard Tetrahedra," *J. Chem. Phys.* 35, 194101 (2011).

[32] P. Damasceno, M. Engel and S.C. Glotzer, "Crystalline Assemblies and Densest Packings of a Family of Truncated Tetrahedra and the Role of Directional Entropic Forces," ACS Nano, 6 (1), pp 609–614 (2012). Publication Date (Web): November 19, 2011

[33] P.F. Damasceno, M. Engel and S.C. Glotzer, "Predictive Self-Assembly of Polyhedra into Complex Structures," Science, 337 453-457, (2012). DOI: 10.1126/science.1220869

[34] M. Balu, J. Hales, D. Hagan, E. Van Stryland, "White-light continuum Z-scan technique for nonlinear materials characterization", Optics Express , 12 #16, 3820, 2004.

[35] Mihaela Balu, Joel Hales, David J. Hagan, and Eric W. Van Stryland, "Dispersion of nonlinear refraction and two-photon absorption using a white-light continuum Z-scan", Optics Express, 13, No. 10, 3594-99, 2005.)